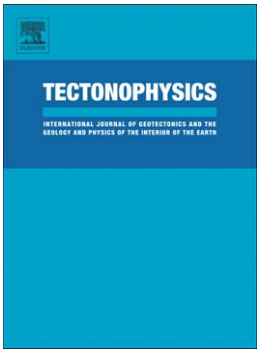

Tectonic and gravity-induced deformation along the active Talas-Fergana Fault, Tien Shan, Kyrgyzstan

A. Tibaldi, C. Corazzato, D. Rust, F.L. Bonali, F.A. Pasquarè Mariotto, A.M. Korzhenkov, P. Oppizzi, L. Bonzanigo

PII: S0040-1951(15)00350-9
DOI: doi: 10.1016/j.tecto.2015.06.020
Reference: TECTO 126664

To appear in: *Tectonophysics*

Received date: 8 August 2014
Revised date: 7 June 2015
Accepted date: 8 June 2015

Please cite this article as: Tibaldi, A., Corazzato, C., Rust, D., Bonali, F.L., Pasquarè Mariotto, F.A., Korzhenkov, A.M., Oppizzi, P., Bonzanigo, L., Tectonic and gravity-induced deformation along the active Talas-Fergana Fault, Tien Shan, Kyrgyzstan, *Tectonophysics* (2015), doi: 10.1016/j.tecto.2015.06.020

Tectonic and gravity-induced deformation along the active Talas-Fergana Fault, Tien Shan, Kyrgyzstan

Tibaldi A.[1], Corazzato C.[1,], Rust D.[2], Bonali F.L.[1], Pasquarè Mariotto F.A.[3], Korzhenkov A.M.[4,5], Oppizzi P.[6], Bonzanigo L.[6]*

[1] *Department of Earth and Environmental Sciences, University of Milan-Bicocca, Italy*
[2] *School of Earth and Environmental Sciences, University of Portsmouth, Portsmouth, U.K.*
[3] *Department of Theoretical and Applied Sciences, University of Insubria, Varese, Italy*
[4] *Institute of Physics of the Earth, Russian Academy of Sciences, Moscow, Russia*
[5] *Institute of Communication and Information Technologies, Kyrgyz-Russian Slavic University, Bishkek, Kyrgyzstan*
[6] *Geolog.ch Ltd, Viale Stazione 16A, Bellinzona, Switzerland*

Abstract

This paper shows, by field paleoseismological data, the Holocene activity of the central segment of the intracontinental Talas-Fergana Fault (TFF), and the relevance of possible future seismic shaking on slope stability around a large water reservoir. The fault, striking NW-SE, is marked by a continuous series of scarps, deflected streams and water divides, and prehistoric earthquakes that offset substrate and Holocene deposits. Fault movements are characterised by right-lateral strike-slip kinematics with a subordinate component of uplift of the NE block. Structural, geological and geomorphological field data indicate that shallow and deep landslides are aligned along the TFF, and some of them are active. Where the TFF runs close to the reservoir, the fault trace is obscured by a series of landslides, affecting rock and soil materials and ranging in size from small slope instabilities to deep-seated gravity-induced slope deformations (DGSD). The largest of these, which does not show clear evidence of present-day activity, involves a volume of about 1 km^3 and is associated with smaller but active landslides in its lower part, with volumes in the order of $2.5 \cdot 10^4$ m^3 to $1 \cdot 10^6$ m^3. Based on the spatial and temporal relations between landslides and faults, we argue that at least some of these slope failures may have a coseismic character. Stability analyses by means of limit equilibrium methods (LEM), and stress-strain analysis by finite difference numerical modelling (FDM), were carried out to evaluate different hazard scenarios linked to these slope instabilities. The results indicate concern for the different threats posed, ranging from the possible disruption of the M-41 highway, the main transportation route in central Asia, to the possible collapse of huge rock masses into the reservoir, possibly generating a tsunami.

[*] Corresponding author. Now at: Department of Earth Sciences "A. Desio", University of Milan, Italy. E-mail: claudia.corazzato@gmail.com

Keywords

Active fault; Landslide; Deep-seated slope deformation; Tien Shan; Talas-Fergana Fault

1. Introduction

The Talas–Fergana Fault (TFF) is a 700-km-long WNW- to NW-striking structure, bisecting the central Tien Shan mountains (Fig. 1). Although displaying classic features of active strike-slip faulting and being clearly expressed on satellite images, the fault is poorly accessible and known, in part because of its position at the border territory between China and the former Soviet Union. Previous studies were mostly based on remote sensing image interpretations and description of offset landforms, which indicate large Holocene displacements (Tapponnier and Molnar, 1979; Trofimov, 1984; Makarov, 1989; Trifonov et al., 1990; Burtman et al., 1996; Mamyrov et al., 2009). However, although all authors agree on significant Holocene offsets along the TFF (review in Simpson et al., 1981), only a couple of studies have been published, in Russian, on the distribution of landslides along this fault (Korjenkov, 1997; Strom, 2009), despite recognition that large active faults in mountain settings may be associated with both shallow and deep-seated slope failures. Several researchers infer a generic relationship between active faults and slope failures (e.g. Cotton, 1950; Keefer, 1984, 1999; Dramis et al., 1994; Rodríguez et al., 1999; Kellogg, 2004; Eusden et al., 2005; Gutiérrez et al., 2007), whereas other authors stress the structural control of major faults on the location of deep-seated gravity-induced slope deformations (DGSD) (e.g. Tibaldi and Pasquarè, 2008).

In Kyrgyzstan, the TFF crosses the Toktogul reservoir, impounded by a reinforced concrete dam, 214 m high and 293 m wide, and located in the steep, narrow gorge of the Naryn River (Fig. 2). The dam was completed in 1975 with a maximum reservoir capacity of 19.5 km^3. The reservoir is 65 km long and 12 km wide at its widest point, and has a surface area of 284 km^2. The maximum depth of the reservoir is 200 m. From the dam, the reservoir follows the Naryn River northeastwards until it crosses the TFF and opens into the main part of the reservoir. Along the SW shore, the reservoir abuts directly against the trace of the TFF (Simpson et al., 1981) (Fig. 2). The strategic importance of the Toktogul reservoir is linked to the fact that it constitutes the major source of energy production in Kyrgyzstan, and the waters of the Naryn River irrigate the highly populated (some 10 million people) Fergana Valley in Uzbekistan (Fig. 1). Of major concern is the possibility that a landslide collapse into the water reservoir might induce a tsunami, although calculation of the direction of propagation and run-up of the related waves are beyond the scope of the present work.

No previous studies have been published in English on the assessment of the stability of the slopes surrounding the Toktogul Lake. A few studies, published in Russian, were carried out during

the feasibility and design stages of the reservoir, but they do not show any numerical assessment of slope stability (Kagan et al., 1976; 1980). These studies suggest some stability problems along the slopes of the narrow Naryn River gorge, but we could not include this zone in our field study due to safety restrictions near the dam. Only some regional studies on landslides have been done (Shibakova et al., 1992; Belousov et al., 1994; Strom, 1996; Havenith et al., 2003a,b; Havenith et al., 2006; Havenith and Bourdeau, 2010). However, it is well known that landslides can be triggered by strong earthquakes, in the Tien Shan and elsewhere (e.g. Ghose et al., 1997; Bogachkin et al., 1997; Havenith et al., 2000, 2003b; Abdrakhmatov et al., 2003).

Our study aims to assess whether slope instability exists around the shores of the Toktogul reservoir, including under possible dynamic conditions. To achieve this aim we provide new data on: 1) the presence of incremental fault displacements along the TFF in correspondence of the Toktogul lake, indicating important paleoseismic activity, and 2) the presence of deep and shallow landslides along the TFF and their activity status along and close to the Toktogul lake. Based on the integration of these observations, we quantify the slope failure potential under static and pseudo-static (seismic shaking) conditions. We use field geological, structural, paleoseismological, geomorphological and geomechanical data to describe the characteristics of the TFF and related landslides. Limit equilibrium and stress-strain analyses were performed with inputs from field and published data, including information on the Peak Ground Acceleration (PGA) (Abdrakhmatov et al., 2003) and derived seismic coefficients.

2. Tectonic and geological setting

The Tien Shan range represents an actively deforming orogenic belt, some 2500 km long, 300-500 km wide, and with elevations up to 7.5 km, which lies between the relatively stable Kazakh and Turan Platforms to the north and the Tarim Basin (Fig. 1) to the south. Deformation was initiated in late Tertiary times as a result of Indian – Eurasian collision, and recent GPS data indicate North-South shortening of about 20 mm/y, representing some 40% of present day Indian – Eurasian collision (Abrakhmatov et al, 1996; Midi and Hugger, 2001; Zubovich et al., 2010). Regional structures formed in response to this deformation are dominantly reverse, E-W-striking faults (Fig. 3). However, the TFF is a right-lateral strike-slip structure that cuts obliquely across the range, forming the largest strike-slip fault in central Asia.

The TFF has a history that began as early as Palaeozoic times (Burtman et al., 1963; Rolland et al., 2013), although significant activity commenced much later, particularly after the collision of India and Eurasia. Most studies of deformation in the Tien Shan conclude that neotectonic movements are accelerating (e.g. Trofimov, 1984; Burchfiel et al., 1999; Chen et al., 2002;

Charreau et al., 2006; Sobel et al., 2006), although some authors argue that Quaternary sedimentation increase can be attributed to climate change at Pleistocene times (Zhang et al., 2001; Liu et al., 1996). It seems clear that the TFF is intimately related to Tien Shan deformation and in this respect the work of Makarov (1989) indicates that the TFF juxtaposes Palaeozoic rocks to the southwest (Turbin et al., 1963) with younger sediments of a mega-syncline occupied by the Toktogul depression. Restoration of the continuity of these structures suggests 12-14 km of slip on the TFF (Makarov, 1989). This 12-14 km slip estimate is in good agreement with an earlier estimate of 9-14 km by Rantsman and Pshenin (1967) based primarily on drainage reconstructions, and both studies consider that the most recent reactivation of slip postdates the formation of extensive and deeply entrenched late Pliocene fan complexes, found for example bordering the fault in the Toktogul depression, which represents the onset of molasse-style sedimentation in the region. By considering a longer time window, Burtman et al. (1996) used palaeomagnetic determinations on early Cretaceous deposits and offset dated rocks to evaluate the cumulated offset, concluding that the total right-lateral slip on the TFF has been 50-100 km in the Cenozoic.

The recent deformation along this fault has been studied by several scientists over the past few decades, with a number of works appearing in English (Simpson et al., 1981; Burtman et al, 1987, 1996; Makarov 1989; Trifonov et al., 1990, 1992; Korzhenkov et al., 2013). There is clear evidence of surface faulting events with river channel offsets (in the order of 25-100 m), along tens of km long faults, characteristics that are typical of large magnitude earthquakes (McCalpin, 1996). Trifonov et al. (1990), by dating deposits dammed by the TFF movements, suggest a value of 3-6 m for single-event displacements, produced by M > 7.5 events, and calculate an average late Pleistocene – Holocene slip rate of 5-17 mm/y. Using these values they propose that large magnitude events have a recurrence interval of approximately 600-800 ys. Based on an epicentral macroseismic study of the destructive M_s 7.6 Chatkal earthquake of 1946, Leonov (1960) and Ulomov et al. (2002) assigned this event to a secondary branch of the major TFF, known as the Atoinok thrust fault (Fig. 3). Much older and poorly documented earthquakes may also be related to the TFF (Chedia, 1986).

3. Tectonic activity along Talas-Fergana Fault system

3.1 General structure of the Talas-Fergana Fault

The TFF system extends from WNW-ESE to NW-SE for over 700 km across Kazakhstan and Kyrgyzstan and extends farther southeast into China (Fig. 1) (Burtman et al., 1963, 1996; Rantsman, 1975; Nevsky, 1994). The TFF belongs to a series of major intracontinental faults that accompanied also the Pliocene-Quaternary N-S shortening of this mountain belt by means of

transpressional displacements (Tibaldi and Graziotto, 1997; Tibaldi et al., 1997; Tibaldi, 1998). Seismological data indicate that the TFF is of lithosphere-scale, extending to a depth of 50-60 km (Mamyrov, 2001). The fault zone is recognizable both on satellite images and in the field, and displays clear evidence of recent faulting events (Korjenkov et al., 2006). Along the TFF, other faults showing recent motion have also been recognised (Trifonov et al., 1990; Abdrakhmatov et al., 1994; Burtman et al., 1996; Thompson et al., 2002; Korjenkov, 2006), and show different orientations and kinematics with respect to the TFF. They display mostly reverse offsets (Fig. 3), and locally abut directly against the main TFF zone.

In the Kyrgyzstan study area, the TFF shows a continuous surface trace with a strike ranging N116°-138° from NW to SE (Fig. 2). It crosses a series of E-W-trending mountain ranges, but along the fault trace there are also mountain ranges that parallel the TFF. In the northwestern and southeastern parts of the segment imaged in Figure 2, the fault trace runs mostly along the valley bottoms, whereas in the central segment the fault trace can be followed mostly along mountain slopes. Figure 5A, as an example, portrays the surface fault trace where it crosses a slope northwest of the Toktogul reservoir. Along this fault, river gullies are systematically offset in a right-lateral sense. In Figures 5B and 5C, representing the fault segment located southeast of the Toktogul reservoir, a 1 meter to a few meters high uphill-facing scarp is visible. This scarp faces to the SW consistently with the relative uplift of the SE tectonic block. As in other parts of the studied TFF, this minor component of uplift is accompanied by a much larger component of transcurrence, as imaged in Figure 5D with the systematic right-lateral offsets of gullies and water divides. We performed several surveys along the TFF, including the excavation of a trench for paleoseismological investigations, in order to establish the Holocene activity of the fault that will be described in the following sections.

3.2 Paleoseismology

Detailed observations of offset landforms have been carried out along the fault segment studied. Measurement of offset fossil landforms, such as water divides and gullies, gives cumulative fault displacement. Attention was paid to the typical morphological evolution of river channels: they can abandon their offset lower channel to spill spontaneously over the fault zone and cut a new channel (Wallace, 1968). This river reorganisation can develop into an alignment of upstream and downstream segments of former parallel channels, leading to a connection between channels across the fault trace with no apparent offset. Alternatively, downstream channels of adjacent rivers can capture an upstream channel (Gaudemer et al., 1989), leading to a connection between an upstream segment and the downstream segment of its neighbour, suggesting an apparent offset opposite to the

sense of motion on the fault. All this is strongly influenced by the characteristic spacing of gullies, which in turn is a function of the hydrology and lithology of the area. In areas with the same lithology and hydrology, river lengths and valley widths grow with time. Gaudemer et al. (1989) observed that along several active strike-slip faults, river offsets vary, suggesting that rivers may respond differently to the perturbation of their geometry caused by faulting, depending on the age of the valley. Thus, in order to minimize possible errors, along the TFF we did several measurements of all landform offsets in order to have statistically robust data. We used differential GPS to have the highest precision for each measurement, with an error that can be estimated in the order of a few decimetres of offset measurement. Field data have been taken by measuring the altitude difference and horizontal distance between homologous piercing points, represented by the point of deflection of river gullies and interrupted water divides. These gave us the dip-slip and strike-slip components of offset. By considering a vertical attitude of the fault, as shown by the rectilinear fault trace in plan view, it has been possible to calculate for each pierced point the net-slip, as the square root of the sum of squared vertical and horizontal offsets, and the pitch assumed as the angle between the fault strike and the net-slip vector.

Near the Kokbel' pass, the results indicate that all along the fault segment portrayed in Figure 2, landforms have been systematically displaced with two components: a dominant right-lateral strike-slip offset, up to 135.7 m, and a minor dip-slip component, up to 12.5 m, with relative uplift of the NE block (Fig. 6 and Table 1). It can be noticed that most strike-slip offsets are in the range of 40-92 m, although a few lower and higher values are present. Where both measures were possible, we calculated the resulting net-slips that amount to 40.5-136 m, and derived the pitch angle (5.3° on average, ranging from 2.3° to 10.4°).

As in several other similar high mountain ranges, the presence of systematically offset river streams and water divides suggests Holocene faulting (Gaudemer et al., 1989; Winter et al., 1993; McCalpin, 1996; Tibaldi and Romero, 2000; Rovida and Tibaldi, 2005; Tibaldi et al., 2007). This is mostly based on the assumption that the fault-slip increments occur at a faster rate than the river capacity to rectify its offset bed. Given the altitude of the studied area in Kyrgyzstan (between 1400 and 2500 m a.s.l.) and the presence of glacial deposits of the Last Glacial Maximum (LGM) at very high altitudes, it can be deduced that the offset gullies here studied were mostly formed in the post-LGM period. If we use the average value of net offset (74.19 m) and the post-LGM water run-off starting at 16 ky BP, we obtain a slip-rate in the order of 4.6 mm/y. Although these values are comparable with the fault slip rates of Burtman et al. (1996), we believe that the studied gullies might have started to form also prior to 16 ky BP, thus these slip rates might be overestimated. In any case, our results suggest Holocene tectonic activity along the studied segment of the TFF.

In the vicinity of the reservoir shoreline, analysis of aerial photos taken before reservoir filling, together with field work, have allowed us to recognize faulting of a series of Quaternary alluvial fans (Fig. 7). These fans show uphill-facing scarps that cannot be explained by river erosion or other natural exogenous phenomena. The fault scarps have different heights based on the different portions and age of the offset alluvial fans (Fig. 7B). The greatest heights correspond to the oldest alluvial fan surfaces, whose relative age is based on their morphology and stratigraphic relations. We excavated a trench across the fault in the older alluvial fan (Fig. 8), which revealed the presence of two faults offsetting a sequence of sedimentary fluvial-debris units. The oldest unit is represented by a coarse conglomerate with boulders of half a meter size, which is exposed only on the NE tectonic block, consistently with the observation that the fault scarp faces SW. The bedding shows a sudden tilting towards SW close to the fault plane, suggesting possible drag effects consistent with relative uplift of this block. On the NE block, above the conglomerate unit there is a silty deposit with clasts up to 15 cm in diameter. An erosion surface marks the passage to the soil layer. This succession is in tectonic contact (fault) with a meters thick silty deposit with clasts. Another fault plane marks the passage to the SW tectonic block that shows a sequence of deposits given by: a silt and clasts layer at the bottom, a 80-cm-thick silty sand deposit, a 60-cm-thick silt deposit with very rare clasts, a 10-cm-thick fine conglomerate unit, and an erosion surface with above the modern soil layer. The most recent faulted unit (the silt deposit with very rare clasts) has been dated by Optically-Stimulated Luminescence (OSL), in the absence of palaeosols here, at the Oxford Luminescence Dating Laboratory (University of Oxford, by J.-L. Schwenninger). The result gives an age of 2617 ± 430 ys BP, indicating late Holocene activity along this segment of the TFF.

Further data showing the recency of activity on the TFF come from other offset dated palaeosols. Korjenkov et al. (2012) suggest that a strong earthquake occurred along the Toktogul segment of the TFF about 2400 ys ago, based on dated colluvial wedges found in a series of artificial pits excavated along the fault. Probably the same earthquake also left signs in the Kyldau River (site A in Fig. 1), where a major event was dated at 2320 ± 40 ys BP, and in the Pchan River (site B in Fig. 1), where the paleoearthquake is dated between 2180 ± 120 ys and 2540 ± 70 ys BP (Korjenkov et al., 2012). If these field indications are related to the same seismic event, the extent of the coseismic dislocation was 150–200 km. Theoretically this is possible, and the indicated rupture length is consistent with a similar rupture length associated with the well studied Kebin (Kemin) earthquake of 1911 (M = 8.2) in Northern Tien Shan (Bogdanovich et al., 1914). Korjenkov et al. (2012) also suggest that another earthquake occurred along the same segment of the TFF about 5 ka ago.

Field surveys along the southern shore of the reservoir coast do enable subsidiary faults to be recognised (Fig. 9A). These are arranged into two sets, one striking NW-SE (N119°-160°) and the other striking NNE-SSW (N15°) (Fig. 9B); both sets show transcurrent-oblique (transtensional) motions with average pitch angles of 45°. Comparison with the classic simple shear model suggests these may represent Riedel and Riedel 1 shears, respectively, linked to the main TFF (Fig. 9A). In the apparently subsided zone between these faults there is a series of parallel, N112°-striking, fissures; these reach the surface and have been filled by cm-sized clasts (Fig. 9C and Fig. 9D, right part). This infill is unconsolidated, and at the surface is marked by a small elongate depression. These fissures affect rock masses of Palaeozoic age and thus cannot be considered an effect of jointing due to static loading and sediment compaction. The possibility that they may represent gravitational effects must also be disregarded because they strike parallel to the slope dip. Instead, we regard these fissures as tectonic in origin, related to secondary effects of faulting, since the fissures and the main NW-SE faulting are sub-parallel. The presence of extensional fissuring and transtensional motion is consistent with the general orientation of these subsidiary faults with respect to the main trace of the TFF.

3.3 Seismicity

Seismicity of TFF has been addressed by several authors (Suvorov, 1964; Nersesov et al., 1988; Pavlovet et al., 1989; Trifonov et al., 1990; Moldobekov et al., 1991; Belenovich et al., 1991; Yudahin et al., 1991; Peltzer et al., 1996; Molnar et al., 2000; Abdrahmatov et al., 2002; Djanuzakov et al., 2003; Korjenkov, 2006; Nurmanbetov, 2006), but none have compared historical and instrumental seismic data with paleoseismic information obtained by artificial trenches excavated across the main fault trace. The database used covers the period 1475-2005 AD and combines catalogues from the Institute of Seismology NAS KR, the Seismological Bureau SUAR PRC, and Djanuzakov et al. (2003). Along the entire TFF, the catalogue indicates that during the period 1475-2005, 123 earthquakes with $M_s \geq 4.3$ occurred, although attention should be paid to the estimation of the magnitude and location for the older events, and for this reason we will focus on the most recent earthquakes. The strongest is the Chatkal earthquake of 1946 (Fig. 4A) with M_w = 7.6, and a seismic moment $M_0 = 1.1 \cdot 10^{20}$ N·m, the epicentre of which is confined to the northwestern segment of the fault, although this earthquake has been attributed to the Atoinok fault, a branch of the main TFF (Ulomov et al., 2002). Epicentres of earthquakes of $M_w \geq 4.3$, for the period 1930-2005, are confined mainly to the northwestern and southeastern segments of the TFF (Fig. 4). The central segment is characterized by relatively weak seismicity. The majority of hypocenters in the last 50 ys are confined to a depth of 5-10 km (48%), followed by a depth of 10-

20 km (34%) and, finally, a depth of 20-40 km (18%) (data repository at the Kyrgyz Institute of Seismology).

Focal mechanisms by Belenovich et al. (1991) indicate that in the northwestern segment of the TFF, the P axis is sub-horizontal and the T axis is subvertical, with thrust and combined thrust and strike-slip determinations. In the central segment, the P and T axes are almost subhorizontal and movements of strike-slip type occur. The southeastern segment is characterized by subvertical inclination of the P axes and by sub-horizontal T axes, corresponding to normal and oblique normal faulting.

To evaluate the possible gravity-instability of the slopes surrounding the Toktogul reservoir we needed the seismic coefficient as an input of the analyses. This coefficient can be obtained from the Peak Ground Acceleration (PGA) (see Section 4.2.2). In the absence of a deterministic, site-specific map of the maximum PGA obtained for all the earthquakes recorded in the the region and ascribed to the TFF activity, whose calculation and needed input data were beyond the aim and logistic possibilities of this work, we referred to the probabilistic work of Abdrakhmatov et al. (2003). They suggest that the choice of the prediction period depends upon the geological engineering application. For our problem we include all maximum hazard components implying a PGA value of 0.5 g for upper prediction G-R, Pe85, and 10% probability of exceedance in 100 years. For this kind of important infrastructure, represented by the dam-reservoir system, a 250-year period with a 10% probability of exceedance may even be more adequate, which implies a maximum PGA of 0.7 g, all other parameters kept identical (Abdrakhmatov et al., 2003).

4. Landslides

4.1 General features and field data

The central segment of the TFF is associated with numerous deep-seated slope deformations, rockslides and shallow landslides, as well as increased erosive activity and debris flows. Such phenomena can be observed on both sides of the fault trace. Also several very large landslide-dammed lakes exist along the TFF. A notable example in the northwest is the Sarychelek lake, located 17 km from the fault (7 in Fig 4A), 6200 m in length, 600-1800 m wide and over 320 m deep, formed in prehistoric times through damming of the Karasu river by a mega-landslide of about 2 km^3, with a run-out distance of 8 km (Chedia, 1986). Its proximity to the epicentral zone of the Chatkal earthquake (1946, M_s = 7.6) (Fig. 4A) suggests a seismically-triggered origin (Strom and Korup, 2005).

We report here the results of our investigations of gravity-induced deformation occurring along the TFF in the study area (Fig. 2). To the SE, within the fault segment between the Toktogul

reservoir and Kokbel' pass (Fig. 10A), 14 shallow landslides coincide with the trace of the TFF (Fig. 11A). They range in size from 10 m to 150 m in width, and from 20 to 270 m in length. All of them are located northeast of the surface fault trace and 10 out of the 14 have headscarps coincident with the surface fault trace, clearly demonstrating the mechanical control exerted by the fault plane as a major rock discontinuity. The upper scarps of the other four landslides are located within a few tens of metres from the TFF. Most of these landslides involve the first few metres of Quaternary deposits, mainly represented by colluvium and soil, and the underlying bedrock (Fig. 11B-C). When only the Quaternary deposits are involved, the landslide body is a few metres thick (e.g. in Fig. 11C); where the substrate is also involved the maximum depth of the slip plane is in the order of 30 m (Fig. 11D).

Further NW along the reservoir shoreline, several Quaternary morphostructures suggest gravity instability (Fig. 10). The morphostructures belong to two main types of gravity-induced deformation of different size: i) small shallow landslides (*Type 1*), and ii) medium-sized deep-seated gravity-induced slope deformations (DGSD) (*Type 2*) (Figs. 10A and D). We performed also a field survey in a wider area as we noticed the presence of other uphill- and downhill-facing scarps, and double crests (Fig. 10A). Anyway, these morphostructures are more eroded and discontinuous, possibly suggesting they represent remnants of older and more extensive slope instabilities. Due to their difficult interpretation, these morphostructures have not been included in the present study.

Type 1 failures have typical dimensions in map view from 50 x 50 m to 300 x 300 m. The vertical thickness of these features might be in the order of a few tens of metres at maximum, corresponding to volumes in the order of $2.5 \cdot 10^4$ m^3 to $1 \cdot 10^6$ m^3. They involve both surface deposits (slope debris and soil) and weathered rock substrate (Fig. 10C). These landslides vary from shallow sliding to rotational type. They are typically located close to the shoreline, with the upper scar located close to the maximum level reached in the past by the reservoir, and retrogressive failure of the upper scar has occurred locally. The previously illustrated Kokbel' pass landslides can also be ascribed to the category of *Type 1* instabilities.

Type 2 failures exhibit typical dimensions in map view of 1000 x 1000 m to 2000 x 2000 m. These instabilities are DGSD, because the thickness of the involved rock mass might be in the order of hundreds of metres and extend deeply into the underlying bedrock. Two of these structures, DGSD 1 and DGSD 2, have been picked out in the southwesternmost part of the reservoir coast, in proximity of the mouth of the dam gorge (Figs. 10A and 10D). It is worth noting that they do not show clear evidence of present, or very recent activity; they are distinguished by a series of morphostructural features that probably encompasses a broad zone of past instability. DGSD 1 (Fig. 10B), the largest one, measures 2 x 2 km in map view, and involves the slope up to a maximum

altitude of 1400 m a.s.l. A comparison with the topographic map published before reservoir filling, indicates that the relative relief of the involved rock mass is about 730 m, and if we hypothesize an average thickness for the DGSD of about 250 m, the resulting volume estimate for the whole rock mass is about 1 km^3. It is noteworthy that the largest and most active landslides of *Type 1* are located precisely at the lower part of this DGSD (Fig. 10C-D). DGSD 1 is delimited upslope by a headscarp a few tens of metres high and about 2 km long (Fig. 12A), and this scarp is linked to two well defined rectilinear valleys, trending NE-SW, which define the lateral limits of the DGSD. The basal failure plane of the DGSD daylights below the present reservoir level, and a survey using a small boat suggests it is marked by a white sediment-laden groundwater outflow visible in the water column. Sampling of the white outflow indicated clay-rich material very similar to the fine part of the cataclastic and deeply-altered rocks found onshore (Figs. 12D and 12E).

The rock succession involved in this DGSD is characterised by a dominant regional dip towards the SW, with variable dip angle (Fig. 13). Beginning the lithological description from the lowest exposed stratigraphic levels, i.e. from NE to SW, the rock succession is represented by a range of pervasively fractured lithologies. The published geological map of the area (Turbin et al., 1963) indicates only calcareous rocks (at the 1:200,000 scale of the map); our larger scale field mapping of the succession identified marbles, low-grade meta-sandstones and phyllites. Marbles dip about 50° to the SW, with the dip angle locally increasing (Fig. 12C). Farther to the SW deformed low-grade meta-sandstones and phyllites dip at higher angles (75-85°), before giving way to calcareous rocks rich in belemnites and other fossils. The contact area between these upper calcareous rocks and the phyllites shows intense deformation, open centimetre to decimetre sized folds, and widespread striated fault planes (e.g. Fig. 12B). A cataclastic breccia zone is also present and, in total, the cataclastic plus the ductile deformation zones have a thickness of about 60 m. The dip angle of the upper calcareous rock succession decreases from 85° adjacent to this fault zone, to 45°, although retaining the SW dip. The fault zone shows reverse dip-slip motions, although the dip angles are 80-85°. All these data suggest the presence of an older, important reverse fault zone that has been rotated to its present position. Further SW, the rock succession maintains a 45-50° dip, but the dip direction rotates from SW to W. The upper calcareous rock succession shows only a very slight metamorphic overprint suggesting that metamorphism decreases southwestwards, i.e. towards the upper part of the stratigraphic succession.

Based on the lithologies involved in the instability, which include phyllites that in general have poor geomechanical characteristics, and on the presence of widespread brittle structures, as well as the orientation of morphostructures compatible with past slope instability, and the proximity of the active TFF, we suggest that DGSD 1 has the potential to be reactivated during a large

earthquake. In view of this we have performed a stability analysis of these slopes under static and pseudo-static conditions (earthquake triggering), which will be described in the following sections.

Northwest of the Toktogul reservoir, the surface trace of the TFF is again marked by a few subsidiary parallel and sub-parallel faults (Fig. 14). Along the fault zone, 33 landslides have been recognized, mostly of *Type 1*. The maximum length of the area affected by each landslide ranges in map view from a few tens of metres to 350 m. Four landslides are coincident with the fault trace, while all the others are located at a distance < 1.5 km from the fault.

4.2 Stability analyses

We address the stability and possible failure mechanisms of both *Type 1* and *Type 2* landslides, mindful of the different possible threats they pose. These range from disruption of the M-41 highway to reactivation and possible collapse of DGSD 1 into the Toktogul reservoir triggering a tsunami. While *Type 1* instabilities in the Kokbel' pass area were investigated by limit equilibrium methods (LEM), the main *Type 2* instability of the area, DGSD 1, was analysed by means of both LEM and stress-strain finite difference numerical analyses (FDM) along a two-dimensional cross-section (Fig. 15), assuming plane strain conditions. Both methods are further specified in the following subsections.

4.2.1 Geological-technical conceptual models and input data

Type 1 instabilities in the Kokbel' Pass area

Type 1 landslides involve loose cover and weathered rock substrate along the TFF trace (Fig. 11). Our field surveys revealed a slope dip range from 35°-40° and a geometry compatible with circular failure mechanisms. The age of these landslides is unknown, but based on available ^{14}C dating (SOAN-7026 240±50 yr, in Korjenkov et al., 2010; Korjenkov et al., 2012), they are more recent than 240-370 ys BP. The lithological and stratigraphic characterization of the soils involved in *Type 1* shallow instabilities close to the Kokbel' Pass area (Fig. 11A) was carried out based on available outcrops (e.g. Figs. 11C, 11D). The surficial portion, a few metres-thick, is represented by a granular residual soil covering a weathered and intensely fractured rock substrate. The geotechnical characteristics of these soils and weak rocks were estimated based on in-situ observations and are reported in Table 2. These data were included in a representative simplified slope-perpendicular NNE-SSW cross-section 470 m wide and 315 m high, with a slope angle of 40° (Fig. 16A).

Type 2 instabilities: DGSD 1

The conceptual model used for DGSD 1 is represented by the NE-SW cross-section in Figure 15. This includes three main geotechnical units: i) Fossiliferous calcareous rocks (FC), ii) Phyllites and meta-sandstones (PS), and iii) Marbles (MA). The latter is affected by the TFF zone (FZ), which is here regarded as a separate cataclastic gauge unit. To the NE, the level of the Toktogul reservoir has a range between a minimum of 860 m and a maximum of 890 m a.s.l., based on the elevation of the reservoir in Zyryanov and Antipova (2000). Geomechanical parameters of the rock masses involved in DGSD 1 were obtained from the literature and from comparison of previous data with in-situ observations (Table 3). The complex structural relationships, together with the lack of direct measurements and the substantial tectonisation along and near the TFF suggest the use of conservative best-estimate values for the input parameters.

4.2.2 Limit equilibrium analyses

Method and data input

The LEM is a standard and well established engineering geological procedure for slope stability analysis, and consists of calculating the forces acting on a potential slide surface and the strength available on that surface. The ratio of resisting forces (strength) to disturbing forces (applied load favouring, or "driving", instability) defines the Factor of Safety (FS) (Hoek, 2007). For stable slopes FS is > 1, because resisting forces overcome disturbing forces. At limit equilibrium (FS = 1), since disturbing and resisting forces are equal, the average tensional state along the slide surface lies in the failure envelope of the material, and the slope is on the point of collapsing. A FS < 1 indicates that failure occurs. Additionally, Hoek (2007) suggests a conservative assessment of slope stability as follows: inherently unstable (1 < FS < 1.3), moderately unstable (1.3 < FS < 1.5) and stable (FS > 1.5). In the cases studied, strengths are defined based on a Mohr-Coulomb strength law. Finally, it is important to note that LEM is based on the following assumptions: i) a perfectly rigid body and rigid-plastic behaviour; ii) slope failure takes place as sliding of a mass along a surface; iii) at failure, the strength of the mass is completely mobilised along the entire surface.

The analyses were carried out using the code SLOPE/W (GEO-SLOPE International Ltd, 2010) and applying the Janbu Simplified method (Janbu, 1973). This method tends to be more conservative than others, which is justifiable for hazard assessments (Hungr et al. 1989). The analysis of *Type 2* instabilities also benefited from a specifically developed software (Bonzanigo, 1999) that includes the improvements to the Janbu method suggested by King (1989). In the analysis, the sliding mass is segregated into discrete slices on which slide forces act. Several sets of simulations considered trial slip surfaces generated automatically, for which the associated FS were

computed by an iterative algorithm (GEO-SLOPE International Ltd, 2010). Then, fully-specified slip surfaces were considered.

Along with deterministic trials, where reasonable values of material properties were kept constant (Tables 4 and 5), LEM results were also assessed by probabilistic analyses. Probabilistic analyses are performed to assess the probability of failure (FS < 1), expressed by cumulative probability distribution functions of the resulting FS. The input parameters (material properties, Tables 4 and 5) were sampled using the Monte Carlo method and an appropriate statistical distribution. Sensitivity analyses involve a series of calculations to determine the influence over the FS (and thus on stability) due to systematical variations in a parameter over its specified range, while keeping all other variables constant (Hoek, 2007). To this regard, we also focused on the effect of the possible seismic coefficients using pseudo-static analyses.

Both dry and saturated conditions were taken into account. A tension crack, dry or filled with water, was introduced, and different hydrogeological conditions were assumed by setting up different configurations of the hypothetical piezometric surface (water table), as well as different reservoir levels for the DGSD 1 case (Fig. 15), also from dry conditions to extreme cases of possible heavy surface recharge due to intense precipitation.

Finally, to account for seismic conditions, a pseudo-static approach was applied. This was possible because the materials involved are expected not to lose significant strength during cyclic loading (Seed, 1978; Wyllie and Mah, 2004). The method is based on limit equilibrium analysis whereby inertial forces produced by seismic shaking are represented by a steady force acting at the centroid of each model slice in a horizontal direction out of the face. The effect of this force is to diminish the factor of safety because the shear resistance is reduced and the displacing force is increased. This inertial force is equal to the weight (W) of the potentially unstable mass (and thus of the slice) multiplied by an appropriate semi-empirical dimensionless seismic coefficient (k), expressed as the ratio of the pseudo-static acceleration (a_h) and the gravity acceleration constant (g), as follows:

$$F_h = \frac{a_h}{g} W = k_h W$$

Although two possible components exist (horizontal, k_h, and vertical, k_v), it is generally considered acceptable to ignore the vertical component of the ground motion in the analysis (Wyllie and Mah, 2004). In fact, in the case that this vertical component is in phase with, and has the same frequency as, the horizontal component, the effect of incorporating the vertical component will not change the FS by more than about 10%, provided that $k_v < k_h$ (NHI, 1998; Wyllie and Mah, 2004).

There is no simple method for determining an appropriate value for the seismic coefficient, which should correspond to a fraction of the predicted PGA (Kramer, 1996; CDMG, 1997; Melo and Sharma, 2004), in combination with a FS of 1.0-1.2 (CGS, 2008). In engineering practice this fraction is typically assumed to be 0.5 times the horizontal PGA (Hynes-Griffin and Franklin, 1984; Wyllie and Mah, 2004), according to Newmark's (1965) method for computing permanent displacements of slopes under seismic shaking. While Marcuson and Franklin (1983) suggest one third to a half of the PGA, the results of Melo and Sharma (2004) indicate k_h values 40-45% of the horizontal PGA. Finally, Pyke (2010) proposes a range of 0.2-0.5 times the PGA to back relate the seismic coefficient to earthquake magnitude in the range 6.5-8, based on Makdisi and Seed (1977) and Seed (1978). Therefore, taking into account these suggestions, and considering the PGA values of Abdrakhmatov et al. (2003) of 0.5 g and 0.7 g for return periods of 100 and 250 years respectively, and of known earthquake magnitudes in the area such as those produced by the Kashgar (M_w = 7.7) and Chatkal (M_w = 7.6) events, we considered a k_h range of 0.1–0.35. The highest values in the range describe the largest expected seismic events in the study area for these return periods, whereas a value of 0.15 simulates a more probable earthquake event with a shorter return period. Both deterministic and sensitivity analyses were carried out using these values.

LEM results for Type 1 instabilities at Kokbel' Pass

This stability analysis was conducted along the section shown in Fig. 16A, and using the probabilistic distribution of geotechnical properties shown in Table 2. Both critical circular slip surfaces automatically searched with an iterative method and a fully-specified slip surface (Fig. 17A) were considered. In the first case, the software searches for all the possible circular surfaces and calculates for each of them the FS; among these, only the meaningful ones are then considered in the analysis (Fig. 16). In the second case, the most reasonable failure surface is drawn in based on expert judgment and the associated FS is calculated. For both cases, along with the FS for each deterministic trial, a probability distribution function for FS, and the associated probability of failure (PF, where FS = 1) were calculated. The hydrogeological conditions examined ranged from totally dry to fully saturated, including the effect of recharge due to heavy rains.

The results, shown in Figures 16-17 and Table 4, reveal instability of the slopes along the Kokbel' Pass valley, with landsliding both in case of hydraulic overloading, and seismic shaking. Soil slip along shallow planar surfaces, with thicknesses of about 10 m, can occur even in dry conditions and with empty tension cracks (TC), always producing FS < 1 (Tab. 4). Failures involving greater thicknesses (20-30 m) are at limit equilibrium conditions (FS ~ 1-1.15), even in dry conditions and empty TC (Fig. 16C). Surfaces involving all the soil cover (Unit 1) down to the

contact with the weathered and fractured bedrock (Unit 2), in dry conditions have FS > 1. When the TC is filled and a seismic coefficient k_h = *0.15* is applied, FS ~ 1, suggesting limit equilibrium conditions (Fig. 16D). When a fully-specified slip surface is drawn according to field evidence and expert judgment, with the tension crack at the slope break corresponding to the TFF trace, and the slip surface at the contact between Unit 1 and the fractured bedrock of Unit 2 (Fig. 17A), the slope is stable in dry conditions, as well as with a TC filling of 50%. The probability of failure rises to 7.95% when TC is fully filled. When a k_h of 0.15 is applied, the dry case reaches a probability of failure of 27.1%, of 56.6% when the TC is filled by half, and nearly 100% when completely filled (Fig. 17B). A sensitivity analysis was then performed for k_h in the range 0.1-0.35, first keeping constant the chosen deterministic values for material properties, and then repeated for another set of minimum values (Table 2). Results show that in the first case FS < 1 for values of k_h < 0.155, while in the second case FS < 1 for values of k_h < 0.1 (Fig. 17C).

Several cases of possible piezometric surfaces were also considered to account for different hydrogeological conditions, and in particular to account for possible surface recharge due to intense precipitation (Fig. 17D and Table 4). When the piezometric surface affects Unit 2 only (WT 2), FS is always > 1 (Table 4). With a convex piezometric surface that also involves part of the bottom of Unit 1 (WT 3), the probability of failure is still 0%, but when the TC is completely filled with water the probability rises significantly to 62%. When applying a k_h value of 0.15, the probability is 77.6%, and 100% when coupled with a completely filled TC (Fig. 17D). With a convex groundwater level above the contact between the two units (WT 1), and Unit 1 partially saturated, especially at the foot of the slope (with a spring in the sliding mass), and intending to model a likely reduction in the shear strength at the basal sliding surface, the probability of failure is 68.5%, and rises to 100% when either the TC is filled or k_h = 0.15 is applied (Fig. 17D). When considering a slope-parallel piezometric surface, 30-40 m deep and involving the lower half of Unit 1 (WT 4), the probability of failure is 5.7%. When either the TC is completely filled or a k_h of 0.15 is applied, the probability of failure rises dramatically to 100% (Fig. 17D). Both a piezometric surface nearly coincident with topography (WT 5), or one fully saturating the slope (WT 6), give a failure probability of 100% (Table 4).

The effect of also considering the vertical component of the seismic coefficient in the pseudo-static analyses was also tested, taking $k_v = k_h$, but the change in the resulting FS was negligible and far less than 10%, in agreement with that observed in general by NHI (1998).

LEM analysis of DGSD 1

The aim of this analysis was to find which sets of geomechanical parameters (friction angle and cohesion) and hydrodynamic conditions would produce a critical value (close to 1) for FS, both in static and pseudo-static conditions, as well as sensitivity to the seismic coefficient value. Actually, a DGSD is considered to be always at the limit equilibrium, although in reality it may experience some creep movement. The velocities of the unstable mass are high in phases of critical activity, and very low in near-stable conditions, as confirmed by the general understanding of such landslides (Cronin, 1992; Bonzanigo, 1997; 1999; Bonzanigo et al., 2007; Eberhardt et al., 2007). The operation is unfortunately not unique, since in the search for limit equilibrium through "back-analysis", an increase in hydraulic load corresponds to an enhancement of the strength parameters. Similarly, some of the geometrical parameters could be varied, but the most reliable slide surface (Figs. 15 and 18A) is obtained by comparison with other deep seated landslides. In particular, the slide zone usually develops with a subvertical tension crack (TC), in agreement with those observed during our surveys and on aerial photographs, which then descends as a curving listric surface hundreds of metres deep. Such geometry is explained by the deviation at depth of the preferential directions of shear forces, and the transformation of active pressures to passive pressures (Ramsay and Huber, 1987). No direct information is available on the position of the slide surface, but for such a DGSD in crystalline rocks, deformation can be expected to be distributed across a several-metres-wide shear zone where shear mechanical processes occur, interacting with mechanical and hydrodynamic conditions. This can be regarded as viscous behaviour, which only approximately can be approached by limit equilibrium methods (Bonzanigo et al., 2000; 2001; 2007; Eberhardt et al., 2007).

In the analysis, deterministic trials were examined for four different sets of geotechnical properties, from intact to extensively altered rock and with different properties of the cataclastic fault zone, ranging in the worst case considered to an extremely porous cohesionless gauge material (Table 5). Different scenarios of hydrogeological and hydrodynamic conditions were also hypothesised, with different lake levels (860 m and 890 m a.s.l.), and associated with a flat piezometric surface, or with a 20 m or 80 m hydraulic head along the slide surface (Fig. 18). Pseudo-static conditions were simulated with k_h = 0.15, and a sensitivity analysis was performed in some of the cases within the range 0.1-0.35. The input conditions and the results, in terms of FS and critical value of *k*, are presented in Figure 18 and Table 5.

When considering properties of Set 1 (Table 5), limit equilibrium conditions are reached only with a hydraulic head of 80 m, a full TC and k_h = 0.15. Set 2 introduces very poor properties for the fault zone, but this has little effect on the results. More interestingly, Set 3 considers much reduced geotechnical parameters (due to alteration) for the rock masses, and involves the shear zone

where deformation occurs. This produces limit equilibrium conditions with a dry or flat piezometric surface, when the TC is full or k_h = 0.15 is applied. The variation in the hydrodynamic conditions show that the change in lake level alone does not influence greatly the FS for the theoretical sliding surface (Table 5), unless the model is already close to a limit equilibrium, in which case such a change can act as a destabilizing factor. When coupled with a 20 m or even 80 m hydraulic head of dynamic overpressure along the slide surface, with a circulation gradient that is equal to the dip of the surface itself (Fig. 18F), the FS decreases. This case is the most realistic in explaining the instability (FS < 1) of the deep-seated landslide with the hypothesized geometry, associated with a k_h = 0.15. This can represent, to a first approximation, the condition of temporary pore overpressure, dynamically triggered by seismic shaking, and explaining the activation of the sliding surface in case of a high intensity earthquake.

Further simulations were then carried out that considered deterministic trials on automatically searched critical circular slip surfaces, comparable to *Type 2* and *Type 1* landslides along the lake shore (Fig. 19), with altered material properties, as Set 4 in Table 5, and with TC filled, both in static and pseudo-static (k_h = 0.15) conditions. Results show that *Type 2* in static conditions have FS > 1 (Fig. 19A), and FS < 1 (Fig. 19B) only when a seismic coefficient is applied. *Type 1* instability (FS < 1) is greatly affected by the alteration and the saturation of the materials from the reservoir waters, inducing failure even in the absence of seismic loading (Fig. 19 C). The loading, when applied, results in even more unfavourable scenarios (Fig. 19D).

4.2.3 Stress-strain analysis

The stress-strain analysis was carried out along the slope affected by DGSD 1, using the FLAC 6.0 code (Fast Lagrangian Analysis of Continua; Itasca Consulting Group, 2008). This code is based on the explicit finite difference method, where elementary cell subdivision and elastic-plastic behaviour are assumed, and the solution proceeds through iteration. It models a non-linear system evolving in time, where deformation and progressive failure can be monitored during the step process, and progressive plasticisation areas can be recognised, providing local yield information. The analysis was performed along the entire cross-section of Figure 15, with a horizontal extent of about 4000 m and a total height of 1600 m. Such an extended model is required to avoid possible boundary effects in the area of interest. The model, assumed as a continuum, is represented by a finite difference grid of 210 x 60 cells (totalling 12600 cells), with an average resolution of 20 m (ranging 12.5-26.5 m), adjusted to fit the topography and the main units. The boundary conditions are obtained by fixing both x- and y-velocities at zero at the sides and base of the model. The equilibrium states are achieved under gravity conditions. The model includes four

main lithotechnical units (Fig. 15), whose physical-mechanical properties are defined in Table 3. Reservoir water load on the submerged slope was taken into account, and the hydrogeological conditions were assumed by introducing two different configurations of the water table (hypothetical piezometric surface), from a horizontal table coincident with the lake level at 890 m a.s.l. (WT0) to a convex shaped one (WT1) with a maximum depth of 400 m beneath the slope and gently connecting to the reservoir water level (Fig. 15). The latter could represent the extreme case of high surface recharge due to intense precipitation. Saturation conditions were imposed to the grid nodes located below the water table, which provided a pore pressure distribution corresponding to a static head below a specified phreatic surface, while no water flow was simulated. The effective stress (σ') field is calculated according to the Principle of Effective Stress: $\sigma' = \sigma - u$, where σ is the total stress and u is the pore water pressure (Terzaghi, 1936; Terzaghi et al., 1996).

A parametric analysis was carried out to evaluate the role played by different sets of physical-mechanical properties and by different piezometric configurations on the stress-strain behaviour of the slope (Fig. 20). Initial conditions are represented by relatively good material properties (Table 3, values in bold are "intact") while a second set takes into account possible deep weathering of the rock mass and the fault zone, producing an extremely porous and cohesionless gauge material with reduced strength and deformation parameters. The simulation was implemented through different stages, as shown by the plot of the maximum unbalanced forces (Fig. 20A), which consider the progression of the analysis through a series of calculation steps and equilibrium states. Equilibrium is considered to be reached when unbalanced forces become stationary. Fig. 20B shows pore pressure distributions for the different water table configurations. For each stage, the results of the simulations are expressed in terms of stress and strain fields, displacement and velocity patterns, plasticity states and shear strain increments.

In the first stage of each simulation the equilibrium state under elastic conditions was achieved (EL in Fig. 20A) by applying gravity acceleration after having assigned elastic properties to the units. This enabled the stress configuration due to the geometric arrangement of the system to be determined, as well as preparing for subsequent perturbations. In the second stage (MC1 in Fig. 20A), the Mohr-Coulomb constitutive law was chosen for the units, and strength properties were assigned to each material region according to Table 3 (values in bold = "intact"). With this set of properties, in static conditions and with a static and flat water table (WT0), no relevant deformation mechanism develops, although at slope breaks the contours of shear strain increments highlight possible localised areas of shallow instability (Fig. 20C). The third stage (MC2 in Fig. 20A) introduced values for altered (weathered) Mohr-Coulomb strength and deformability properties (Table 3; values in bold = "altered"). At equilibrium, although no general mechanism involving the

entire DGSD 1 develops, the contours of maximum shear strain increments, coupled with displacement and velocity vectors (show in figure inset), highlight the development of relatively small shallow-seated areas of instability. These are marked by yield in shear, one between 1150 m and 1320 m a.s.l., involving a mass with a thickness of about 40 m and a downslope extent of about 350 m, and another close to the reservoir shore at about 1000 m a.s.l. with a thickness of about 30 m. Both consistent with observed *Type 1* failures (Fig. 20D). These *Type 1* failure mechanisms are further highlighted when the piezometric level is raised from WT0 to WT1, although not leading to general failure of the entire DGSD 1 (Fig. 20E). Similar effects are obtained when additional degradation of the properties of the highly tectonized PS unit is introduced.

5. Discussion

5.1 Possible origin of the slope deformations

Along most of the studied TFF there are a series of aligned slope failures that range from small surface landslides to deep-seated collapses. Although aligned landslides along an active fault might be typically triggered by seismic shaking (e.g. McCalpin, 1996, and references therein), a major uncertainty derives from the fact that triggering might be related to other causes of non-tectonic origin. These causes may include severe atmospheric perturbations that can enhance gravity-induced instability by water saturation of soils and rock fractures, snow melting due to climate change, anthropogenic activities and erosion (e.g. Tibaldi et al., 1995, and references therein). Anthropogenic effects can be ruled out due to the remoteness of the area, and extreme weather events are here very rare although they cannot be totally excluded. A key question is reconstruction of the age of the slope failures along the fault trace in order to assess whether they have the same age and thus may have been generated by the same event, such as an earthquake. There are several examples of landslides triggered by earthquakes along faults in Kyrgyzstan, such as the landslides developed during the 1992 earthquake of Kochkor-Ata (M_s 6.3) (Fig. 4A), the debris slumps in the Suusamyr valley and rock avalanches in the Aramsu and Suusamyr Ranges triggered by the Suusamyr earthquake in 1992 (M_s 7.3) (Fig. 4A), the rock avalanches in the Kyrgyz Range triggered by the Belovodsk earthquake in 1885 (M_s 6.9) (Fig. 4A), and the rock avalanches in the Chon Kemin and Chon Aksu valleys triggered by the 1889 Chilik (M>8.0) and 1911 Kemin (M_s 8.2) earthquakes (Fig. 4A) (Abdrakhmatov et al, 2003).

Work on seismically-triggered landslides in Central Asian mountain regions has been carried out by Havenith and Bordeau (2010) and Havenith et al. (2013a, b), who considered the interaction between regional seismic hazard and local geological conditions, combining field work with distinct element numerical modelling. They concluded that large magnitude seismic events (M

≥ 7) in the Tien Shan and northern Pamir, with return periods of 20 years, were capable of triggering most of the observed giant rockslides, while smaller earthquake events were considered enough to trigger earth-flows or shallow landslides. Although these shallow landslides present smaller involved volumes than massive rock avalanches, their higher spatial and temporal occurrence, probably related to shorter earthquake return periods (ranging up to a few years), contribute to them being a significant geological hazard (Havenith and Bordeau, 2010).

In high mountain environments DGSD are also considered to be produced by slope debuttressing following fusion/retreat of valley glacial tongues (e.g. Berrisford and Matthews, 1997; Holm et al., 2004). Along the studied parts of the TFF glaciation did not affect the valleys, and thus post-glacial debuttressing cannot be claimed as a triggering mechanism.

Holocene DGSD aligned along active faults are also interpreted as being triggered by earthquake ground shaking, and the fault trace is seen as a predisposing major zone of weakness along which rock mass detachment occurs; this has been proved, for example, in Alpine settings along the Engadine Fault (Tibaldi and Pasquarè, 2008). The landslides that we studied are coincident with the trace of the TFF, or at only a short distance from it. Although we are aware that absolute dating of each landslide is missing, we think that diverse past climatic conditions or ancient earthquakes might have played a triggering role. In order to verify this suggestion, we collected a series of organic-rich sediments from trenches and pits that we excavated in lacustrine deposits from now-breached landslide-dammed lakes, close to the TFF. This will allow us to establish if the DGSDs in the area were linked to prehistoric earthquakes (Rust et al., in prep.). More significantly, near the Toktogul reservoir we collected new data suggesting strong paleoseismic activity, which could have triggered the landslides and that will be described in the next section.

5.2 Coseismic fault deformation

In proximity of the reservoir, we recognised faulting of a series of Quaternary alluvial fans (Fig. 7). The different heights of the fault scarps affecting alluvial fan surfaces of diverse ages indicate that incremental fault displacement occurred here, and suggest a long history of multiple paleoseismic events. The trench we excavated across the fault trace (Fig. 8) reveals the presence of faults offsetting a sequence of sedimentary units. The oldest units are exposed on the NE tectonic block, consistent with morphological observations of the fault scarps facing SW, and the general uplift component of the NE block observed everywhere. Also the drag folding of the strata is consistent with relative uplift of the NE block. The age of the most recent offset unit indicates that the last seismic event along this segment of the TFF occurred after 2617 ± 430 ys BP. This age is

consistent with other findings by Korjenkov et al. (2012) in other sites along the fault, suggesting that a strong earthquake occurred between 2180 ± 120 and 2540 ± 70 ys BP.

Since the area has been affected by river erosion, the succession of deposits here is not complete. The absence of the unit dated 2617 ± 430 ys BP on the upthrown block may be interpreted as due to a previous seismic event that created an older scarp (that allowed the deposition of this unit only in the downthrown block); an alternative interpretation may explain the lack of the unit dated 2617 ± 430 ys BP, as a consequence of erosional processes. Therefore, the dip-slip component of 1.5 m for the faulting event recognized in the trench should be considered a maximum value. From the offset-magnitude relationship for dip-slip faults of Papazachos et al. (2004), we obtain an estimated value of the moment magnitude (M) of 6.9. In order to calculate a more reliable M based on the net slip, in view of the important strike-slip component along the TFF suggested by field observations and focal mechanism solutions, we use measurements carried out at the conterminous surface fault trace. We consider the cumulative dip-slip and right-lateral strike-slip components measured closer to the trench site (Figure 6, Table 1) that give a reconstructed average pitch of 7°. Using this pitch to calculate the net slip at the artificial trench, we obtain a maximum value of 12 m, and from the offset-magnitude relation for strike-slip faults of Papazachos et al. (2004), we obtain an estimated maximum value of the $M \geq 8$ at this segment of the TFF. The value of 12 m is consistent with the right-lateral strike-slip offsets of small (young) gullies of 13-16 m that we measured along the close segment of the TFF.

Although we are aware of the uncertainty linked to this reconstruction of M, we argue that the trench study clearly indicates that this segment of the TFF does not move by creeping but by incremental coseismic offsets, and that an earthquake with M between 6.9 and 8 occurred after 2617 ± 430 ys ago. We conclude that since this phenomenon took place in the very recent history of the area, it is plausible that strong seismic shaking along the shores of the Toktogul reservoir might also occur in the future, and justifies the calculations we will discuss in the following section. Also the other field data collected at the conterminous fault segments, as well as the seismological data resumed in this paper, indicate that the TFF is a major active structure that deserves attention for possible seismic hazard.

5.3 Stability assessment of slope deformations

Field observations enable correlations between geological conditions and landslide occurrence to be established. We then performed LEM and stress-strain numerical analyses to assess the influence of individual geological and seismic factors on slope stability in a complex geological-structural framework. The input parameters of the models were varied in order to assess

the sensitivity of the results. This approach revealed that the numerous landslides of *Type 1* aligned along the TFF, near the Kokbel' Pass, involving the loose cover and the weathered and intensely fractured rock substrate on steep slopes, are generated (via circular failure mechanisms) by both hydraulic overloading and seismic shaking. We distinguished different possible landslides, from shallower ones, involving only the loose cover, to deeper ones, involving all the cover down to the contact with the fractured bedrock. Shallow (10 m) soil slips along planar surfaces can occur even in completely dry conditions, due to the unfavourable characteristics of the materials involved and the presence of discontinuities along the fault that serve to promote tension cracks. Slope instabilities with slip surfaces involving greater thicknesses (20-30 m) are inherently unstable (limit equilibrium conditions), which means that rainfall or very weak seismic loading could trigger the destabilisation. Deeper surfaces, extending to the contact with the fractured bedrock and involving thicknesses in the order of 60-70 m (Figs. 16D and 17A), observed locally in the field (Fig. 10D), are stable in dry conditions, even when a reasonable range in material properties is considered. However, they become inherently unstable when the headwall tension crack is completely filled with water, with a probability of failure of about 8% (Table 4). An earthquake loading corresponding to a seismic coefficient k_h of 0.15 has a similar effect, with the probability of failure increasing to 27%. The probability of failure raises dramatically to 100% when earthquake load is coupled with the effect of a rise in water level and/or filling of tension cracks (Fig. 17D, Table 4). The effect of also considering, in pseudo-static analyses, the vertical component of the seismic coefficient, taken as $k_v = k_h$, produces a negligible change in the resulting FS, far less than 10% and in agreement with that observed in general by NHI (1998).

When considering DGSD 1, there is no clear evidence of present-day activity. However, the presence of diffuse fractures in the rock mass, the lithological and mechanical characteristics of the rock masses involved, and the slope dip, are all predisposing characteristics that warrant carrying out a quantitative assessment of the potential for gravity-induced failure. The coupled results of LEM and stress-strain modelling indicate that two crucial variables in instability are rock-mass properties and structure. While with relatively favourable properties (Set 1, Table 5) the slope is always stable, or moderately unstable in case of partial saturation and seismic loading (k = 0.15); less favourable geomechanical properties represent a long-term influence that significantly affects stability. This is due to both weathering and substantial tectonisation/fracturing (Set 4), especially within the fault zone (FZ), which is regarded as a cataclastic, porous and cohesionless gauge unit, and within the subvertical phyllites and meta-sandstones (PS). These unfavourable rock-mass properties, coupled with locally steep slopes and the presence of the reservoir, lead to moderately unstable conditions and predispose the development of *Type 1* shallow-seated landslides along the

slope. This occurs even in static conditions and with a flat piezometric surface, as outlined by SSI contours combined with displacement and velocity vectors from stress-strain simulations (Fig. 20D). Surface recharge, represented by a rise in the piezometric level, produces a decrease in the Factor of Safety, but no SSI envelope comparable to a *Type 2* slip surface as a single mechanism develops. Pseudo-static limit-equilibrium analyses show instead the fundamental role of the short-term effect of seismic loading, such as potentially generated by future displacement of the TFF, in developing inherent instability or even failure conditions for DGSD 1 when the hypothesized sliding surface geometry is combined with a rise in the water table (Table 5). This could represent, to a first approximation, the condition of temporary pore overpressure caused by seismic shaking.

In light of these results and the field data summarised in Section 7.1, our work supports the hypothesis that failure or limit equilibrium conditions exist for *Type 1* shallow landslides, such as those recognized in the field. This landslide type, in shallower cases (Figs. 16B,C) involving only the soil cover (Unit 1), could initiate at the slopes considered even in the absence of any seismic load. Conversely, *Type 1* instabilities associated with deeper shear surfaces (Fig. 17A) could also suffer from the effect of water level rise from rainwater recharge (Fig. 17D), although this is less likely to occur due to the generally dry climatic conditions in the area. Our field studies also show that past *Type 1* landslides are exactly aligned along the outcropping surface of the TFF and thus this structure acts as a major mechanical discontinuity guiding the location of the slope instabilities, similarly to that observed, for example, at the Engadina Fault in the Alps (Tibaldi and Pasquarè, 2008). But what is most relevant is that our numerical approach indicates that these landslides could have been easily triggered by seismic loading (Fig. 17B,D).; thus similar processes could occur again downslope of the TFF, associated with earthquake events having seismic coefficients (*k)* in the order of 0.1-0.15 (Fig. 17C). Such landslides could affect the M-41 main highway.

As concerns *Type 2* landslides, the worst-case scenario of seismic loading triggering the collapse of DGSD 1, indicates that a volume of 1 km^3 would impact in the Toktogul artificial reservoir, likely inducing a tsunami. Computation of run-up and direction of wave propagation deserves further analysis, especially in relation to possible channelling effects in the conterminous narrow valley of the Naryn River.

Although only a few other works exist on seismically triggered landslides in central Asia, we believe that much more investigation is necessary, taking into account the wide occurrence of heavily fractured rock, steep slopes and very high relative relief, with several valley bottoms lying from 2000 to 4000 m below adjacent mountain crests. We think that future work should concentrate slope stability analyses of areas with a high potential risk, such as the analyses presented above that

consider the gravity-tectonic threat posed to the M-41 highway linking Kyrgyzstan to Uzbekistan and Tajikistan, and the threat posed to coastal settlements around Toktogul reservoir.

6. Conclusions

We carried out geological-structural surveys, paleoseismological analyses at an artificial trench, aerial photograph interpretation, and stability analyses by limit equilibrium methods and stress-strain modelling, in order to study tectonic and gravity-induced deformation developed along the central segment of the active Talas-Fergana fault, in Kyrgyzstan. This fault strikes WNW-ESE to NW-SE and is marked by a continuous series of scarps, offset streams and water divides, and landslides. Geophysical data indicate the presence of seismic foci for most segments of the fault, although there are no historical records of faulting along the studied segment. The paleoseismological analyses of the trench and the offset alluvial fans of diverse age indicate that repeated coseismic fault displacement has occurred in the Holocene. The last large pre-historic earthquake occurred after 2617 ± 430 ys ago and had a moment magnitude M > 6.9. Based on this, we believe that new large earthquakes might occur in the future along the studied segment of the TFF, with possible landslide triggering. Tens of relatively small shallow landslides in fact, are present along the studied fault segment, as well as some deep-seated slope failures. Given the Holocene age of these landslides, and their alignment along the fault trace, we suggest that at least some of these gravity-induced failures (thus excluding the shallowest ones in very poor soil materials) may have been triggered by seismic shaking. Similarly, future large earthquakes may trigger reactivation of the landslides, or new slope failures.

In particular, along the southwestern shore of the Toktogul reservoir, we applied limit equilibrium methods and performed a stress-strain numerical analysis to evaluate the possible instability factors and the most reliable expected failure mechanisms along the slopes. Static and pseudo-static analyses suggest that a rock mass with a volume of about 1 km^3 is prone to failure only in the event of a large earthquake in the area, corresponding to a seismic coefficient k value ≥ 0.15. This landslide has the potential to generate a tsunami in the Toktogul reservoir, and this possibility deserves further attention.

Acknowledgments

This work was made possible by funding from NATO – Science for Peace project "Geo-environmental security of the Toktogul hydroelectric power station region, central Asia" (TC EAP SFP 983142). This paper is also a contribution to the International Lithosphere Program - Task

Force II. We acknowledge suggestions from two anonymous reviewers, and T. Apuani provided useful discussions on slope stability issues.

References

Abdrakhmatov, K.E., Lemzin, I.N., Strom, A.L., 1994. Neotectonics of the Ketmen'-Tyube depression. In: Chedia O.K. (ed.), The Tien Shan During Epoch of Neotectonic Orogeny. Bishkek Ilim Publ. P. 86-96 (in Russian).

Abdrakhmatov, K.E., Mamyrov, E., Tupchy, Yu.G., Mahankova, V.A., Povolotskaya, I.E., Delvaux, D., 1996. Prognosis of activization of seismicity, landslide processes and atmospheric precipitations on the territory of Southern Kyrgyzstan on the basis of analysis of their quasi-periodicity. Science and new technologies. N4, 58-64 (in Russian).

Abdrakhmatov, K.E., Haveniht, H.B., Delvaux, D., Jongmans, D., Trefois, P., 2003. Probabilistic PGA and Arais Intensity maps of Kyrgystan (Central Asia). Journal of Seismology, 7, 1-18.

Belenovich, T.Y., Sabitova, T.M., 1991. Dynamics of transorogenal fault. In: Recent geodynamics of lithosphere of the Tien-Shan. Moscow, Nauka, 101-105.

Belousov, T. P., Skobelev, S.F., Strom, A.L., 1994. On estimation of the recurrence period of strong earthquakes of the central Tien Shan (according to data of absolute geochronology). Journal of Earthquake Prediction Research, 3, 226-236.

Bogachkin, B.M., Korzhenkov, A.M., Mamyrov, E., Nechaev, Yu.V., Omuraliev, M., Petrosyan, A.P., Pletnyov, K.G., Rogozhin, E.A., Charimov, T.A., 1997. The structure of 1992 Susamyr earthquake source based on its geological and seismological manifestations. Izvestiya. Physics of the Solid Earth, 33, 11, P. 867-882.

Bogdanovich, K.I., Kark, I.M, Korolkov, V.JA., Musket, I.V., 1914. Earthquake in northern chains of Tian-Shan on December, 22nd, 1910 (on January, 4th, 1911). Works of Geological Committee (Geolcom –Геолком), Issue 89, 270 pp.

Bonzanigo, L., 1997. Rheological particularities and artesian heads in a large landslide: successful reclaiming by using of underground drainage. International Symposium of IAEG: Engineering Geology and the Environment, Athens, 1997.

Bonzanigo, L., 1999. Lo slittamento di Campo Vallemaggia. PhD.Sc. thesis, Engineering Geology, Swiss Federal Institute of Technology (ETH Zurich), Zurich, Switzerland. (in Italian. ETHZ electronic library: http://e-collection.library.ethz.ch/eserv/eth:23420/eth-23420-02.pdf).

Bonzanigo L., Eberhardt E., Loew S., 2000. Measured Response to a Drainage Adit in a Deep Creeping Slide Mass. Landslides in research, theory and practice. Ed. by E.Bromhead,

N.Dixon and M-L. Ibsen. Proceedings of the 8th International Symposium on Lanslides held in Cardiff on 26-30 June 2000. Thomas Telford editions.

Bonzanigo L., Eberhardt E., Loew S., 2001. Hydromechanical Factors controlling the Creeping Campo Vallemaggia Landslide. Davos, UEF.

Bonzanigo, L., Oppizzi, P., Tornaghi, M., Uggeri, A., 2006. Hydrodynamics and Rheology: Key Factors in Mechanisms of Large Landslides. In Nadim, F., Pöttler, R., Einstein, H., Klapperich, H., Kramer, S. (eds.), Geohazards. ECI Symposium Series, Volume P7 (2006).

Bonzanigo, L., Eberhardt, E., Loew, S., 2007. Long-term investigation of a deep-seated creeping landslide in crystalline rock. Part 1. Geological and hydromechanical factors controlling the Campo Vallemaggia landslide. Canadian Geotechnical Journal, 44(10), 1157-1180, 10.1139/T07-043.

Burchfiel, B. C., Brown, E. T., Qidong, D., Li, J., Feng, X., Molnar, P., Shi, J., Wu, Z., You, H., 1999. Crustal shortening on the margins of the Tian Shan, Xinjiang, China, Int. Geol. Rev., 41, 663–700.

Burtman, V.S., 1964. The Talas-Ferghana strike-slip fault. Geologicheskiy Institute Trudy, Akademiya Nauk SSSR, 104, 143 pp (in Russian).

Burtman, V.S., Peive, A.V., Ruzhentsov, S.V., 1963. Main faults of Tien Shan and Pamir. In: Proceedings of GIN USSR, 89, 152-172 (in Russian).

Burtman, V.S., Skobelev, S.F., Sulerzhitsky, L.D., 1987. Talas-Ferghana fault: Recent displacements in the Chatkal region in the Tien Shan. Transactions of USSR Academy of Sciences. 296, 5, 1173-1176.

Burtman, V.S., Skobelev, S.F., Molnar, P., 1996. Late Cenozoic slip on the Talas-Fergana fault, the Tien Shan, central Asia. Geol. Soc. Am. Bull. 108, 1004-1021.

Buslov, M.M., Klerkx, J., Abdrakhmatov, K., Delvaux, D., Batalev, V.Yu, Kuchai, O.A., Dehandschutter, B., Muraliev, A., 2003. Recent strike-slip deformation of the northern Tien Shan. Society, London, Special Publication 210, 1, 53-64.

CDMG (California Department of Mines and Geology), 1997. Guidelines for Evaluating and Mitigating Seismic Hazards in California. California Division of Mines and Geology, Special Publication 117. http://ladpw.com/ldd/dmg117slope.pdf

CGS (California Geological Survey), 2008. Guidelines for Evaluating and Mitigating Seismic Hazards in California 2008. California Department of Conservation, California Geological Survey, Special Publication 117A. http://www.conservation.ca.gov/cgs/shzp/webdocs/Documents/SP117.pdf

Charreau, J., Gilder, S., Chen, Y., Dominguez, S., Avouac, J. P., Sen, S., Jolivet, M., Li, Y., Wang, W., 2006. Magnetostratigraphy of the Yaha section, Tarim Basin (China): 11 Ma acceleration in erosion and uplift of the Tian Shan mountains. Geology, 34(3), 181-184.

Chedia, O.K., 1986. Morphostructures and Neotectonic Tectogenesis of the Tien Shan. Frunze: Ilim Publ. 314 pp (in Russian).

Chen, J., Burbank, D.W., Scharer, K.M., Sobel, E., Yin, J., Rubin, C., Zhao, R., 2002. Magnetochronology of the Upper Cenozoic strata in the Southwestern Chinese Tian Shan: rates of Pleistocene folding and thrusting. Earth and Planetary Science Letters, 195(1), 113-130.

Cotton, C.A., 1950. Tectonic scarps and fault valleys, Geological Society of America Bulletin 61, 717-757.

Cronin, V.S., 1992. Compound landslides: Nature and hazard potential of secondary landslides within host landslides. Reviews in Engineering Geology, Geological Society of America, 9, 1-9.

Djanuzakov, K.D., Chedia, O.K., Abdrahmatov, K.E., Turdukulov, A.T., 1996. The map of seismic division into districts of Kyrgyz Republic (scale 1: 1000 000). Bishkek: Ilim, 24 p.

Dowding, C.H., 2000. Construction Vibration. McCormick School of Engineering and Applied Science, Northwestern University USA. Chapter 18.

Dramis, F., Sorriso-Valvo, M., 1994. Deep-seated gravitational slope deformations, related landslides and tectonics. Engineering Geology, 38, 231-243.

Eberhardt, E., Bonzanigo, L., Loew, S., 2007. Long-term investigation of a deep-seated creeping landslide in crystalline rock. Part II. Mitigation measures and numerical modelling of deep drainage at Campo Vallemaggia. Canadian Geotechnical Journal, 2007, 44(10), 1181-1199, 10.1139/T07-044.

Elms, G.E., 2000. Refinements to the Newmark Sliding Block Model. Twelfth World Conference on Earthquake Engineering. http://www.iitk.ac.in/nicee/wcee/article/2132.pdf.

Eusden, J., Pettinga, J.R., Campbell, J.K., 2005. Structural collapse of a transpressive hanging-wall fault wedge, Charwell region of the Hope Fault, South Island, New Zealand. New Zealand Journal of Geology & Geophysics, 48, 295-309.

Fedorenko, V.S., 1988. Landslides and rockfalls in mountains, and their forecasting. Moscow University Press, Moscow, Russia.

Frantz, D., 2000. "Maili Suu Journal: Living at Ground Zero of Possible Atomic Disaster" *New York Times*, 21 October 2000, p. 4; in Lexis-Nexis Academic Universe, http://web.lexis-nexis.com. {Updated 2/16/01 KB}.

Fu, B., Ninomiya, Y., Guo, J., 2010. Slip partitioning in the northeast Pamir–Tian Shan convergence zone. Tectonophysics 483(3), 344-364.

Gaudemer, Y., Tapponnier, P., Turcotte, D.L., 1989. River offsets and active strike-slip faults. Annales Tectonicae, 3, 55-76.

GEO-SLOPE International Ltd, 2010. Stability Modeling with SLOPE/W 2007 Version. An Engineering Methodology. Fourth Edition. Calgary, Canada. 355 pp. www.geo-slope.com.

Ghose, S., Mellors, R.J., Korjenkov, A.M., Hamburger, M.W., Pavlis, T.L., Pavlis, G.L, Omuraliev, M., Mamyrov, E., Muraliev, A.R., 1997. The M_S=7.3 1992 Suusamyr, Kyrgyzstan earthquake in the Tien Shan: 2.Aftershock focal mechanisms and surface deformation. Bulletin of Seismologic Society of America, 87, 1, 23-38.

Ghose, S., Hamburger, M.W., Ammon, C.J., 1998. Source parameters of moderate‐sized earthquakes in the Tien Shan, central Asia from regional moment tensor inversion. Geophysical research letters, 25(16), 3181-3184.

Gutiérrez, F., Bruhn, R.L., McCalpin, J.P., Guerrero, J., Lucha, P., 2007. Evidence of compressional active tectonics in Ragged Mountain Fault (Southern Alaska). European Geosciences Union General Assembly, Geophysical Research Abstracts, Vol. 9, 01780.

Havenith, H.B., Bourdeau, C., 2010. Earthquake-induced landslide hazards in mountain regions: a review of case histories from central Asia. Geologica Belgica, 13/3, 137-152.

Havenith, H.B., Jongmans, D., Abdrakhmatov, K., Trefois, P., Delvaux, D., Torgoev, I.A., 2000. Geophysical Investigations Of Seismically Induced Surface Effects: Case Study Of A Landslide In The Suusamyr Valley, Kyrgyzstan. Surveys in Geophysics, 21 (4), 351-370.

Havenith, H.B, Strom, A., Calvetti, F., Jongmans, D., 2003a. Seismic triggering of landslides. Part B: Simulation of dynamic failure processes. Natural Hazards and Earth System Sciences, 3, 663–682.

Havenith, H.B., Strom, A., Jongmans, D., Abdrakhmatov, K., Delvaux, D., Trefois, P., 2003b. Seismic triggering of landslides, Part A: Field evidence from the Northern Tien Shan. Natural Hazards and Earth System Sciences, 3,135-149.

Havenith, H.B., Torgoev, I., Meleshko, A., Alioshin, Y., Torgoev, A., Danneels, G., 2006. Landslides in the Mailuu-Suu Valley, Kyrgyzstan - Hazards and Impacts. Landslides, 3, 137–147. DOI: 10.1007/s10346-006-0035-2.

Hoek, E., 2007. Practical rock engineering. Online. Ed. Rocscience. https://www.rocscience.com/hoek/corner/Practical_Rock_Engineering.pdf.

Holm, K., Bovis, M., Jakob, M., 2004. The landslide response of alpine basins to post-Little Ice Age glacial thinning and retreat in southwestern British Columbia. Geomorphology, 57, 201–216.

Hynes-Griffin, M.E., Franklin, A.G., 1984. Rationalizing the Seismic Coefficient Method. U.S. Department of the Army. Waterways Experiment Station. US Army Corps of Engineers, Miscellaneous Paper GL-84-13, 21 pp.

Hungr, O., Salgado, F.M., Byrne, M., 1989. Evaluation of three dimensional method of slope stability analysis. Canadian Geotechnical Journal, 26, 679–686

Itasca Consulting Group, 2008. Fast Lagrangian Analysis of Continua (FLAC). Theory and Background. Fourth Edition (FLAC Version 6.0). Minneapolis, Minnesota.

Janbu, N., 1973. Slope stability computation. in: R.C. Hirschfiel and S.J. Poulos (eds.), Embankment-Dam Engineering, John Wiley, 47-86.

Kagan, M.L., Chechot, V.Z., Tutkevich, V.A. 1976. Experience of engineering and geological study of locality of building of the Toktogul Hydro-Power Station. In: Proceedings of Hydroproject, vol. 48, Moscow, Hydroproject Press, 206-218 (in Russian).

Kagan, M.L., Chechot, V.Z., Kayakin, V.V., Molokov, L.A., 1980. Toktogul Dam across the Naryn River. In: Geology and Dams, Vol. VIII, Moscow, Energy Press, 30-45 (in Russian).

Keefer, D.K., 1984. Landslides Caused by Earthquakes. Geological Society of America Bulletin, 95: 406–421.

Keefer, D.K., 1999. Earthquake-induced Landslides and Their Effects on Alluvial Fans. Journal of Sedimentary Research, 69: 84–104.

Kellogg, K.S., 2004. Thrust-induced collapse of Mountains. An example from the "Big Bend" region of the San Andreas Fault, Western Transverse Ranges, California. U.S. Geological Survey Scientific Investigation Report 2004-5206, 16 pp.

Khodzhaev, A., 1985. Paleoseismology of the Chatkal-Kurama Region. Tashkent: Fan Press, 132 pp (in Russian).

King, G.J.W., 1989. Revision of effective stress method of slices. Geotechnique, 39 (3), 497-502.

Kopnichev, Yu.F., Sokolova, I.N., 2003. Spatiotemporal Variations of the S Wave Attenuation Field in the Source Zones of Large Earthquakes in the Tien Shan. Izvestiya, Physics of the Solid Earth, 39, 7, 568–579.

Korjenkov, A.M., 1997. Seismic deformations of the Uzunakhmat river basin – one of manifestation of the Talas-Fergana seismogenic zone. Echo of Science. Proceedings of National Academy of Sciences of Kyrgyz Republic, 4, 30-35 (in Russian).

Korjenkov, A.M., 2006. Seismogeology of the Tien Shan. Bishkek: Ilim, 290 pp.

Korjenkov, A.M., Bobrovsky, A.V., Mamyrov, E., Povolotskaya, I.E., Fortuna, A.B., 2006. Paleoseismic deformations in the Talas-Fergana Fault Zone in the Kyrgyzstan territory. Science and New Technologies, 2, 81-90 (in Russian).

Korjenkov, A.M., Bobrovsky, A.V., Mamyrov, E.M., 2010. Evidence for Strong Paleoearthquakes along the Talas–Fergana Fault Near the Kök-Bel Pass, Kyrgyzstan. Geotectonics, 44, 3, 262–270.

Korjenkov, A. M., Rust, D., Tibaldi, A., Abdieva, S.V., 2012. Parameters of the strong paleoearthquakes along the Talas-Fergana Fault, the Kyrgyz Tien Shan. In: D'Amico, S. (ed.), Earthquake Research and Analysis – Seismology, Seismotectonics and Earthquake Geology. InTech Publishers, Rijeka, Croatia, 33-84. ISBN: 978-953-307-656-0.

Korzhenkov, A.M., Abdieva, S.V., Burtman, V.S., Orlova, L.A., Rust, D., Tibaldi, A., 2013. Indications of Late Medieval Earthquakes in the Talas–Fergana Fault Zone, Tien Shan. Geotectonics, 47, 6, 444–453. ISSN 00168521 (Original Russian Text published in Geotektonika, 47, 6, 84–94).

Kramer, SL., 1996. Geotechnical Earthquake Engineering. Prentice-Hall, Inc., Upper Saddle River, New Jersey 07458, 434-437.

Leonov, NN., 1960. Khait earthquake of 1949 and the geological conditions of its occurrence. Geology and Geophysics, Geophysical Series, 3, 48–56 (in Russian).

Liu, T., Ding, M., Derbyshire, E., 1996. Gravel deposits on the margins of the Qinghai-Xizang plateau, and their environemental significance, Palaeogeogr. Palaeoclimatol. Palaeoecol., 120, 159–170, doi:10.1016/0031-0182(95)00039-9.

Makarov, V.I. 1989. On horizontal displacement along the Talas-Fergana Fault during Neotectonic epoch. Transactions of USSR Academy of Sciences, 308, 4, 932-937.

Makdisi, F.I., Seed, H.B., 1977. Simplified procedure for estimating dam and embankment earthquake-induced deformations. In ASAE Publication No. 4-77. Proceedings of the National Symposium on Soil Erosion and Sediment by Water, Chicago, Illinois, December 12-13, 1977.

Mamyrov, E., 2001. Elastic properties of crystal mountain rock under thermodynamical conditions of earth crust of Tien Shan active fault zones. Bishkek: Ilim, 159 pp (in Russian).

Mamyrov, E., Korzhenkov, A.M, Orlova, L.A., Pogrebnoi, V.N., Rust, D., Strom, A.L., Fortuna, A.B., Bobrovskii, A.V., Grebennikova, V.V., Makhankova, V.A., Nurmanbetov, K., 2009. Geodynamics of the Talas-Ferghana fault in the Tien Shan: natural hazards on the territory of Central Asia". Bishkek, Arashan Press, 230 pp (in Russian).

Marcuson, W.F., Franklin, A.G., 1983. Seismic Design, Analysis, and Remedial Measures to Improve the Stability of Existing Earth Dams - Corps of Engineers Approach. In: T.R. Howard (Ed.), Seismic Design of Embankments and Caverns. New York, ASCE, 1983.

McCalpin, J.P. (ed.), 1996. Paleoseismology. Academic Press, San Diego, CA., 480 pp.

Mellors, R.J., Vernon, F.L., Pavlis, G.L., Abers, G. A., Hamburger, M.W., Ghose, S., & Iliasov, B., 1997. The M_s= 7.3 1992 Suusamyr, Kyrgyzstan, earthquake: 1. Constraints on fault geometry and source parameters based on aftershocks and body-wave modeling. Bulletin of the Seismological Society of America, 87(1), 11-22.

Melo, C., Sharma, S., 2004. Seismic coefficients for pseudostatic slope analysis. 13 WCEE: 13th World Conference on Earthquake Engineering Conference Proceedings, Paper No. 369. http://www.iitk.ac.in/nicee/wcee/article/13_369.pdf

Midi, B.J., Hager, B.H., 2001. Recent distribution of deformation in the western Tien Shan by block models, based on geodetic data. Russian Geology and Geophysics, 42, 10, 1622-1633.

Moldobekov, K.M., Djanuzakov, K.D., 1991. Seismic regime. In: Recent geodynamics of lithosphere of the Tien-Shan. Moscow, Nauka, 113-122.

Molnar, P., Chose, S., 2000. Seismic moments of major earthquakes and rate of shortening across the Tien Shan. Geophys. Res. Letters, 27, 16, 2377-2380.

Nersesov, I.L., Ilyasov, B.I., Pavlov, V.D., Preobrajenskiy, V.B., Ruzaikin, A.I., 1988. Changes of seismicity in the region of Toktogul hydro knot in connection with exploitation of the water reservoir. Frunze, Pub. AN Kyrg. SSR, 4, 82-92.

Nevskiy, M.V., 1994. Superlong-period waves of deformation on boundaries of lithospheric plates. Collection: «Dynamic processes in geophysical medium», M.: Nauka, 40-54 (in Russian).

Newmark, N.M., 1965. Effects of Earthquakes on Dams and Embankments. Géotechnique, 15, 2, 139-160.

NHI (National Highway Institute), 1998. Geotechnical Earthquake Engineering. Publication No. FHWA HI-99-012, Washington DC, 265 pp.

Nurmanbetov, K., 2006. Geological environment and estimation of seismic danger of the Talas-Fergana Fault. Bishkek, Nauka (science) and New Technology. Bishkek, 1, 38-44.

Papazachos, B.C., Scordilis, E.M., Panagiotopoulos, D.G., Papazachos, C.B., Karakaisis, G.F., 2004. Global relations between seismic fault parameters and moment magnitude of earthquakes. Bulletin of the Geological Society of Greece, XXXVI, 1482-1489.

Pavlov, V.D., Pavlova, G.I., Ruzaikin, A.I., Simpson, D., 1989. The study of seismic generation in the region of Toktogul Water Reservoir. In: Geophysical studies in seismodangerous zones. Moscow: Nauka, 90-103.

Peltzer, G., Saucier, F., 1996. Present-day kinematics of the Asia derived from geologic fault rates. J. Geophys. Res., 101, B12, 27,943-27,956.

Pyke, R., 2010. Selection of seismic coefficients for use in pseudo-static slope stability analyses. Consulting Engineer, Lafayette, CA. TAGA Engineering Software Ltd 2010. http://www.tagasoft.com/TAGAsoft/Discussion/article2_html.

Ramsay, J.G, Huber, M.U, 1987. The Techniques of Modern Structural Geology: Folds and Fractures. 521 pp. Academic Press, London, New York.

Rantsman, E.Ya., Pshenin, G.N., 1963. First results of the geomorphologic investigations of horizontal displacements of the earth crust along the Talas-Fergana Fault. Proceedings of USSR Academy of Sciences. Geographical Series, 5.

Rantsman, E.Ya., Pshenin, G.N., 1967. Neotectonic horizontal movements of the earth crust in the Talas-Fergana Fault zone by data of geomorphologic analysis. In: Tectonic Movements and Neotectonic Structures of the Earth Crust. Moscow: Nedra Press, 155-159 (in Russian).

Rantsman, E.Ya., 1975. Mountains of Central Asia. In: Geomorphology of the USSR. Plains and mountains of Central Asia and Kazakhstan. Moscow: Nauka, 93-209 (in Russian).

Rodríguez, C.E., Bommer, J.J., Chandler, R.J., 1999. Earthquake-induced landslides: 1980-1997. Soil Dynamics and Earthquake Engineering, 18: 325-346.

Rolland, Y., Alexeiev, D.V., Kröner, A., Corsini, M., Loury, C., Monié, P., 2013. Late Palaeozoic to Mesozoic kinematic history of the Talas–Ferghana strike-slip fault (Kyrgyz West Tianshan) as revealed by< sup> 40</sup> Ar/< sup> 39</sup> Ar dating of syn-kinematic white mica. Journal of Asian Earth Sciences, 67, 76-92.

Rust, D., Tibaldi, A., Bonali F.L., Korzhenkov, A.M., Pasquarè Mariotto, F., 2015. Paleoseismicity along the Talas Fergana Fault, Tien Shan. In preparation.

Rovida, A., Tibaldi, A., 2005. Propagation of strike-slip faults across Holocene volcano-sedimentary deposits, town of Pasto, Colombia. J. Struct. Geol., 27, 1838-1855.

Seed, H.B., 1979. Considerations in the earthquake-resistant design of earth and rockfill dams. Géotechnique, 29(3), 215-263.

Shibakova, V.S., Sadov, A.V., Strom, A.L., 1992. Engineering geology and remote sensing in the USSR. Episodes, 15, 1, 68-74.

Shubin, V.I., Becker A.Y., Konyukhov A.A., Fayzulin V.G., Korzhenkov A.M., 1992. Open-File Report on Karabura Geological Party on Results of Geological Mapping during 1986-1991. Ivanovka town.

Simpson, D.W., Hamburger, M.W., Pavlov, D.V., Nersesov, I.L. 1981. Tectonics and seismicity of the Toktogul Reservoir region, Kirghizia, USSR. J. Geophys. Res., 97, 345-358.

Sobel, E.R., Chen, J., Heermance, R.V., 2006. Late Oligocene–Early Miocene initiation of shortening in the Southwestern Chinese Tian Shan: implications for Neogene shortening rate variations. Earth and Planetary Science Letters, 247(1), 70-81.

Strom, A.L., 1996. Some morphological types of long-runout rockslides: Effects of the relief on their mechanism and on the rockslide deposits distribution. In: (K. Senneset, Ed.) Landslides. Balkema Publ. Rotterdam. 1877-1982.

Strom A.L., 2009. Rock slides, rock falls and dammed lakes in the Talas-Fergana fault zone. In (E. Mamyrov ed.) "Geodynamics of the Talas-Ferghana fault in the Tien Shan: natural hazards on the territory of Central Asia". Bishkek, Arashan Press, 163-171 (in Russian).

Strom, A.L., Korup, O., 2005. Extremely large rockslides and rock avalanches in the Tien Shan Mountains, Kyrgyzstan. Landslides. 1007/s10346-005-0027-7

Strom, A.L., Nikonov, A.A., 1997. Correlation between parameters of seismogenic ruptures and earthquake magnitude Physics of the Earth, 12, 55-67.

Suvorov, A.I., 1964. The main types of large faults in Kazakhstan and in Central Asia. In: Deep down faults. Moscow: Nedra, 60-74.

Tapponnier, P., Molnar P., 1979. Active faulting and Cenozoic tectonics of the Tien Shan, Mongolia and Baykal regions, J. Geophys. Res., 84, 3425-3459.

Terzaghi, K., 1936. Stability of Slopes of Natural Clays. Proceedings of the 1st International Conference of Soil Mechanics and Foundations, Cambridge, MA, 161-165.

Terzaghi, K., 1950. Mechanism of landslides. In: Paige and Sydney (eds.), Application of geology to engineering practice (Berkey volume). New York, Geol. Soc. America, 83-123.

Terzaghi, K., Peck R.B., Mesri, G., 1996. Soil Mechanics in Engineering Practice, 3rd ed., 412 pp., John Wiley, New York.

Thompson, S.C., Weldon, R.J., Rubin, C.M., Abdrakhmatov, K., Molnar, P., Berger, G.W., 2002. Late Quaternary slip rates across the central Tien Shan, Kyrgyzstan, central Asia. J. Geophys. Res., 107(B9), 2203, doi:10.1029/2001JB000596.

Tibaldi, A., 1998. Effects of topography on surface fault geometry and kinematics: examples from the Alps, Italy, and Tien Shan, Kazakstan. Geomorphology, 24, 2-3, 225-243.

Tibaldi, A., Graziotto, E., 1997. Three-dimensional compressional deformations in the Zailiski Alatau mountains, Kazakstan. Geodinamica Acta, 10 (4), 239-250.

Tibaldi, A., Pasquarè, F., 2008. Quaternary deformations along the 'Engadine–Gruf tectonic system', Swiss-Italian border. Journal of Quaternary Science, 23(5), 475–487.

Tibaldi, A., Romero, J.L., 2000. Morphometry of Late Pleistocene-Holocene faulting in the southern Andes of Colombia and volcano-tectonic relationships. Tectonics, 19, 2, 358-377.

Tibaldi, A., Ferrari, L., Pasquarè, G., 1995. Landslides triggered by earthquakes and their relationships with faults and mountain slope geometry: an example from Ecuador. Geomorphology, 11, 215-226.

Tibaldi, A., Graziotto, E., Forcella, F., Gapich, V.H., 1997. Morphotectonic indicators of Holocene faulting in Tien Shan, Kazakstan, and geodynamic implications. Journal of Geodynamics, 23, 1, 47-64.

Tibaldi, A., Corazzato, C., Rovida, A., 2007. Late Quaternary kinematics, slip-rate and segmentation of a major Cordillera-parallel transcurrent fault: The Cayambe-Afiladores-Sibundoy system, NW South America. Journal of Structural Geology, 29, 664-680.

Trifonov, V.G., Makarov, V.I., Skobelev, S.F., 1990. The Talas-Fergana active right-lateral fault. Geotectonics, 24, 5, 435-442.

Trifonov, V.G., Makarov, V.I., Skobelev, S.F., 1992. The Talas-Fergana Active Right-Lateral Fault. Ann. Tectonicae, 6, 224–237.

Trofimov, A.K., 1984. Materials on stratigraphy of Quaternary sediments in the Saryjaz River basin (the Central Tien-Shan). Tien-Shan Cenozoic geology and recent tectonics. Frunze. Ilim, 3-29 (in Russian).

Turbin, L.I., Turbina, V.I, Aleksandrova, N.V., 1963. Geological Map of USSR, 1:200000 scale. K-43-XIX Sheet. Moscow, Nedra Press.

Ulomov, V.I., Polyakova, T.P., Medvedeva, N.S., 2002. On the Long-Term Prediction of Strong Earthquakes in Central Asia and the Black Sea–Caspian Region. Izvestiya, Physics of the Solid Earth, 38, 4, 276–290.

Wallace, R.E., 1968. Notes on stream channels offset by the San Andreas fault, southern Coast ranges, California. In: Dickinson WR, Grantz A (Eds.), Geological problems of the San Andreas Fault System, Stanford Univ. Publ. Geol. Sci., 11, 6-21.

Yudahin, F.N., Chedia, O.K., Djanuzakov, K.D., Nurmanbetov, K., 1991. Seismogenic zones. In: Recent geodynamics of lithosphere of the Tien-Shan. Moscow: Nauka, 169-178.

Winter, T., Avouac, J.P., Lavenu, A., 1993. Late Quaternary kinematics of the Pallatanga strike-slip fault (Central Ecuador) from topographic measurements of displaced morphologic features. Geophys. J. Int., 115, 905-920.

Wyllie, D.C., Mah, C., 2004. Rock slope engineering. Civil and Mining. Fourth edition. Spon Press, Taylor & Francis Group, London, 431 pp.

Zhang, P., Molnar, P., Downs, W.R., 2001. Increased sedimentation rates and grain sizes 2–4 Myr ago due to the influence of climate change on erosion rates, Nature, 410, 891–897, doi:10.1038/35073504.

Zubovich, A.V., Wang, X.Q., Scherba, Y.G., Schelochkov, G.G., Reilinger, R., Reigber, C., Mosienko, O.I., Molnar, P., Michajljow, W., Makarov, V.I., Li, J., Kuzikov, S.I., Herring, T.A., Hamburger, M.W., Hager, B.H., Dang, Y., Bragin, V.D., Beisenbaev, R.T., 2010. GPS velocity field for the Tien Shan and surrounding regions. Tectonics, 29(6).

Zyryanov, A., Antipova, E., 2000. Optimization of the Syr Darya Water and Energy Uses under Current Conditions. Water and energy complexes of the Syr Darya river basin. In: Daene C. McKinney, D.C., and Kenshimov, A.K. (eds). Optimization of the Use of Water and Energy Resources in the Syrdarya Basin Under Current Conditions. Volume II: National Groups. Central Asia Mission - U. S. Agency for International Development Contract No. PCE-I-00-96-00002-00; Task Order No. 813 (June 2000). pp. 48-101. http://www.ce.utexas.edu/prof/mckinney/papers/aral/00-06-W/00-06-W_eng/Vol-2/Section%202%281-Zyryanov%29.pdf

TABLES

Table 1. Data on offsets of river gullies and water divides along the trace of the Talas Fergana fault.

Table 2. Input data for limit equilibrium analyses of *Type 1* landslides at the Kokbel' Pass. Value ranges as introduced in the probabilistic analysis, in brackets the deterministic values. Pseudo-cohesion was locally observed in situ for Unit 1.

Table 3. Geotechnical characterization of the geological-technical units involved in DGSD 1. In bold, values used in FDM stress-strain analysis: in the "altered" set, the fault zone is considered as an extremely porous and cohesionless gauge material. FC = Fossiliferous calcareous rocks, PS = Phyllites and meta-sandstones, MA = Marbles, FZ = Talas-Fergana fault zone.

Table 4. Results of LEM analysis for *Type 1* instabilities at the Kokbel' Pass (cfr. Figs. 16-17). Material properties report the range used for probabilistic analysis, in brackets the values for deterministic trials. WT = water table (piezometric surface), TC = tension crack, FS = Factor of Safety, PF = probability of failure, auto = automatically searched surface.

Table 5. Synthesis of the examined cases for the *Type 2* instability DGSD 1 (portrayed in Fig. 18): input data, hydrogeological conditions and Factor of Safety (FS) outcomes, along with sensitivity analysis results. FC = Fossiliferous calcareous rocks, PS = Phyllites and meta-sandstones, MA = Marbles, FZ = Talas-Fergana fault zone, WT = water table, γ = unit weight, c = cohesion, ϕ = friction angle. DET = Deterministic, SENS = Sensitivity.

FIGURE CAPTIONS

Figure 1. Shaded relief map of the Tien Shan mountains of central Asia. The dominant East-West structural orientation of the mountain ranges is crosscut by the prominent NW-SE-striking Talas-Fergana Fault (TFF), over 700 kilometres in length. This fault system affects Kazakhstan, Kyrgyzstan and China. Along the fault there is the large Toktogul artificial water reservoir that serves the most important hydroelectrical power station of central Asia. The much larger depression to the SW is the Fergana Valley. A = Kyldau River, B = Pchan River. SRTM from http://srtm.csi.cgiar.org/. The trace of the TFF in Kazakhstan has been taken from Buslov et al. (2003) and Rolland et al. (2013). The trace of the southernmost TFF has been taken from Fu et al. (2010) and Rolland et al. (2013).

Figure 2. Satellite image (Google Earth) showing the studied segment of the Talas-Fergana Fault (TFF) in Kyrgyzstan (location in Fig. 1), whose quite continuous surface trace has a strike ranging N116° to N138° from NW to SE. In the northwestern and southeastern parts of this segment the fault trace runs mostly along the valley bottoms, whereas in the central part the fault trace can be followed along mountain slopes (cfr. Fig. 5). Boxes and photo view angles show location of next figures.

Figure 3. Map of the main Quaternary faults of central Tien Shan. Note the presence of the unique NW-SE-striking right-lateral strike-slip Talas Fergana fault, surrounded by several about E-W-striking reverse faults. Modified after Tapponnier and Molnar (1979), Ghose et al., (1998), Thompson et al. (2002).

Figure 4. *A.* Main historic seismic events (1475-1997) around the Talas-Fergana Fault (TFF, in red), and location of earthquake-triggered slope failures (see text for details): 1—Kyrgyz Range; 2 = Chon Kemin valley; 3 = Chon Aksu valleys; 4 = Suusamyr valley; 5 = Suusamyr Ranges; 6 = Mailuu-Suu valley; 7 = Sarychelek lake. Highlighted in red are the epicentres of the Chilik (1889), Kashgar (1902), Kemin (1911), Chatkal (1946), Kochkor-Ata (1992) and Suusamyr (1992) earthquakes. Blue boxes locate the three segments (northwestern, central and southeastern) of the TFF for which the peculiarities of the seismic regime were examined. Modified after Buslov et al. (2003), integrated with Kopnichev and Sokolova (2003). *B.* Instrumental seismicity recorded between 1960 and 2008 in central Tien Shan. TFF = Talas Fergana Fault, NF = Northern-Fergana Fault, GK = Ghissar-Kokshaal Fault, AI = Atbashi-Inylchek Fault, NL = Nikolaev Line (Fault). Base maps are from the Kyrgyz Institute of Seismology (KIS) archive. Boxes in both maps locate the area of Fig. 1.

Figure 5. *A.* Example of the Talas-Fergana Fault segment where the surface fault trace (triangles) runs parallel to the local slope contour lines, with river gullies (blue lines) systematically offset in a right-lateral sense. Location in Figs. 2 and 14. View towards North, Google Earth image. *B.* and *C.* Photos showing uphill facing scarps ,i.e. facing to the SW, in part due to a small component of uplift of the NE tectonic block (man for scale in circle), *D.* Example of the Talas-Fergana Fault segment located southeast of the Toktogul water reservoir, where it can be appreciated the continuous surface trace (segmented black line, TFF) and the systematic right-lateral strike-slip offset of gullies (blue lines) and of water divides (point and dash lines). Location in Fig. 2.

Figure 6. Cumulative offset measured in the field along the segment of the Talas-Fergana fault between Toktogul Lake and Kokbel' Pass. The right-lateral strike-slip and dip-slip

components, and the net slip are shown. The amounts of offset of river gullies and drainage divides are plotted against the distance along fault strike. Inset shows the location of measurement sites along the fault trace, from NW to SE.

Figure 7. *A.* Aerial photo taken before the reservoir creation and *B.* its interpretation, integrated also with field data showing a series of Quaternary alluvial fans offset by the TFF (from the oldest fan "D" to the youngest "A"). Numbers refer to the different fault scarp heights that are consistent with the relative age of the alluvial fans. Location in Fig. 10A. *C.* Field photo of the fault scarps indicated by arrows.

Figure 8. Photo (*A*) and interpreted log (*B*) of the trench that has been excavated along the newly-recognized fault trace cutting the Quaternary alluvial fans. Age obtained by Optically-Stimulated Luminescence. Location in Figure 7B.

Figure 9. *A.* Map of the faults surveyed along the Toktogul reservoir coast, on the prosecution of the surface trace of the Talas-Fergana Fault (location in Fig. 2 and Fig. 10A). These faults might represent Riedel and Riedel 1 shears, respectively, of the main Talas-Fergana Fault, as in the classical simple shear model shown for comparison. *B.* Schmidt's stereogram, lower hemisphere, of the structures found at the studied outcrop. Here faults strike NW-SE and NNE-SSW, and show transcurrent-oblique (transtensional) motion. The line with diverging arrows represents the orientation of the recent fissure. *C.* Photo and interpretation of the studied outcrop. *D.* Photo and interpretation of a close-up on fissures.

Figure 10. *A.* Map of the Talas-Fergana Fault trace close to the Toktogul water reservoir (Location in Fig. 2). Note that a branch of the main fault cuts across a Quaternary alluvial fan. Crosses indicate the relative upthrown fault block. To the northwest the fault trace is replaced by a series of recent and active landslides. These comprise surficial slope failures (*Type 1*) and deep-seated gravity slope deformation (DGSD, *Type 2*). DGSD 1 and DGSD 2 are the largest and most recent zones of deep instability that we have found. *B.* Photo of DGSD 1, taken from a boat. *C.* Photo of the shallow active landslide located at the foot of the DGSD 1. *D.* Perspective view (Google Earth) from the NE of *Type 1 and Type 2* instabilities.

Figure 11. *A.* Map view over a Google Earth image of the Talas-Fergana Fault (TFF) segment located southeast of the Toktogul water reservoir, where several landslides are aligned along the fault trace, also affecting the M-41 international highway. Location in Fig. 2. *B.* How the slope affected by landslides appears to the SE of Fig. 10A. Arrows indicate the fault trace. *C.* Close-up on the slope failure of Fig. 10B. This slope failure involved the Quaternary deposits and the first metres of the hard rock substrate. *D.* Close-up view of the slope failure affecting the NW area of Fig. 10A. This failure involved also the weathered hard rock substrate for a maximum depth of 30 m of the slip plane. The circle indicates a man for scale, and the arrow the fault trace.

Figure 12. *A.* Google Earth image representing the DGSD 1 (see Fig. 10A). Letters locate the following photos, and the trace of the geological cross-section of Fig. 13 is also indicated. *B.* Photo of one of the several rotated reverse faults, with evident striae, that characterise the rock units. *C.* The lowermost part of the outcropping rock succession is characterised by slight metamorphism and pervasive fracturing. *D.* General view of the lower active landslide. *E.* Below the lake level, a wide plume of white water indicates

the presence of an underwater spring probably located along the slip plane of the lower active landslide of Figure 12D.

Figure 13. Geological cross section of DGSD 1 based on geological and structural field data by the authors. Section trace is in Figure 12A.

Figure 14. Northwest of the Toktogul lake (location in Fig. 2), the surface trace of the TFF is again continuous with a few subsidiary parallel and sub-parallel faults. Along the fault zone, 33 landslides have been recognized, mostly surficial (*Type 1*). Four landslides are aligned exactly along the fault trace, while all the others are located at a distance < 1.5 km from the fault. Box locates Fig. 5A.

Figure 15. Geological–technical conceptual model of DGSD 1 (same section trace of Fig. 13) for limit equilibrium and stress-strain numerical analyses, including: main lithotechnical units (properties in Tab. 3), boundary conditions, hydrogeological and gravity settings. FC—Fossiliferous calcareous rocks, PS—Phyllites and meta-sandstones, MA—Marbles, FZ—Talas-Fergana fault zone (fault gauge).

Figure 16. LEM model and results for *Type 1* instabilities at the Kokbel' Pass, carried out along a representative NE-SW cross-section of the slope (*A*). Unit 1 represents the soil cover, Unit 2 the weathered and fractured bedrock (material properties in Table 2). Result are reported in Table 4. Circular failure surfaces according to Janbu's (1973) method. *B.* shallow surfaces at a depth of 10-15 m show FS < 1 also in dry conditions. *C.* Surfaces involving greater thicknesses (20-30 m) are at limit equilibrium conditions. *D.* Surfaces involving all the soil cover (Unit 1) down to the contact with the weathered and fractured bedrock (Unit 2). FS > 1 unless TC is filled and a seismic coefficient $k_h = 0.15$ is applied, in which case limit equilibrium is reached. TC—Tension crack, FS—Factor of Safety.

Figure 17. LEM probabilistic and sensitivity results for *Type 1* instabilities at the Kokbel' Pass. *A.* The fully-specified slide surface is drawn according to field evidence, with the tension crack at the slope break in correspondence with the TFF trace and the slip surface at the contact with the fractured bedrock. Material properties and results in Tables 2 and 4. *B.* Probability distribution function and probability of failure for the dry case in static or pseudo-static (k = 0.15) conditions, and TC empty to completely filled. *C.* Results of the sensitivity analyses on k_h in the range 0.1-0.35 with average (Janbu) and lowest (Janbu-L) values of material properties. *D.* Probability distribution function and probability of failure for different hydrogeological conditions in static or pseudo-static (k = 0.15) conditions and TC empty to completely filled. TC—Tension crack, WT—Water table (piezometric surface), *k*—seismic coefficient.

Figure 18. Synthesis of the cases examined by limit equilibrium methods for DGSD 1 in static and pseudo-static conditions. Details and results in Table 5. *A.* Cross section with units, fully specified slip surface, slices and tension crack (TC). Location in Fig. 15. *B.* Completely dry. *C.* Water table coincident with the lake level at 860 m. *D.* Water table coincident with the lake level at 890 m. *E.* Lake level at 890 m, with 20 m head along the shear zone. *F.* Lake level at 890 m, with 80 m head along the shear zone Case E and F are the most critical (FS < 1) when altered material properties and seismic coefficient are introduced. *G.* Results of the sensitivity analysis on *k*. FC—Fossiliferous calcareous rocks, PS—Phyllites and meta-sandstones, MA—Marbles, FZ—Talas-Fergana fault zone (fault gauge), FS—Factor of Safety.

Figure 19. Results for different circular surfaces for *Type 2* (*A-B*) and *Type 1* (*C-D*) instabilities in static (left) and pseudo-static (right, k_h = 0.15) conditions. *A. Type 2* instabilities (a number of different possible sliding surfaces is shown) in static conditions have always FS > 1. *B. Type 2* instabilities show a FS < 1 only when a seismic coefficient is applied. *C-D.* On the contrary, *Type 1* instability is greatly affected by the alteration and the saturation of the materials from the reservoir waters, and present failure conditions (FS < 1) even in the absence of seismic loading. FC—Fossiliferous calcareous rocks, PS—Phyllites and meta-sandstones, MA—Marbles, FZ—Talas-Fergana fault zone (fault gauge), FS—Factor of Safety. Piezometric surface is the same WT2 of Figure 18F.

Figure 20. Results of the stress-strain analysis with the finite difference code FLAC 6.0 (Itasca Consulting Group, 2008). *A.* Unbalanced forces resulting from different simulation stages. *B.* Pore pressure distribution, water table and lake water load on submerged free surfaces. WT0—water table coincident with the lake level at 890 m a.s.l., WT1—convex-shaped water table. C. Second stage at equilibrium, with Mohr-Coulomb properties (MC1): contours of shear strain increment (SSI). No relevant overall deformation mechanism develops, although incipient shallow concentrations of SSI are evident at slope breaks (outlined by arrows). *D.* Third stage at equilibrium, with degraded Mohr-Coulomb strength and deformability properties (MC2): the contours of shear strain increment coupled with displacement vectors (inset) highlight the development of relatively small shallow-seated areas of instability, marked by yield in shear and consistent with *Type 1* instabilities observed in the field. E. A rise in the piezometric level from WT0 to WT1 leads to a general enlargement of the areas affected by *Type 1* instabilities, but do not evidence the development of a global failure mechanism for DGSD 1.

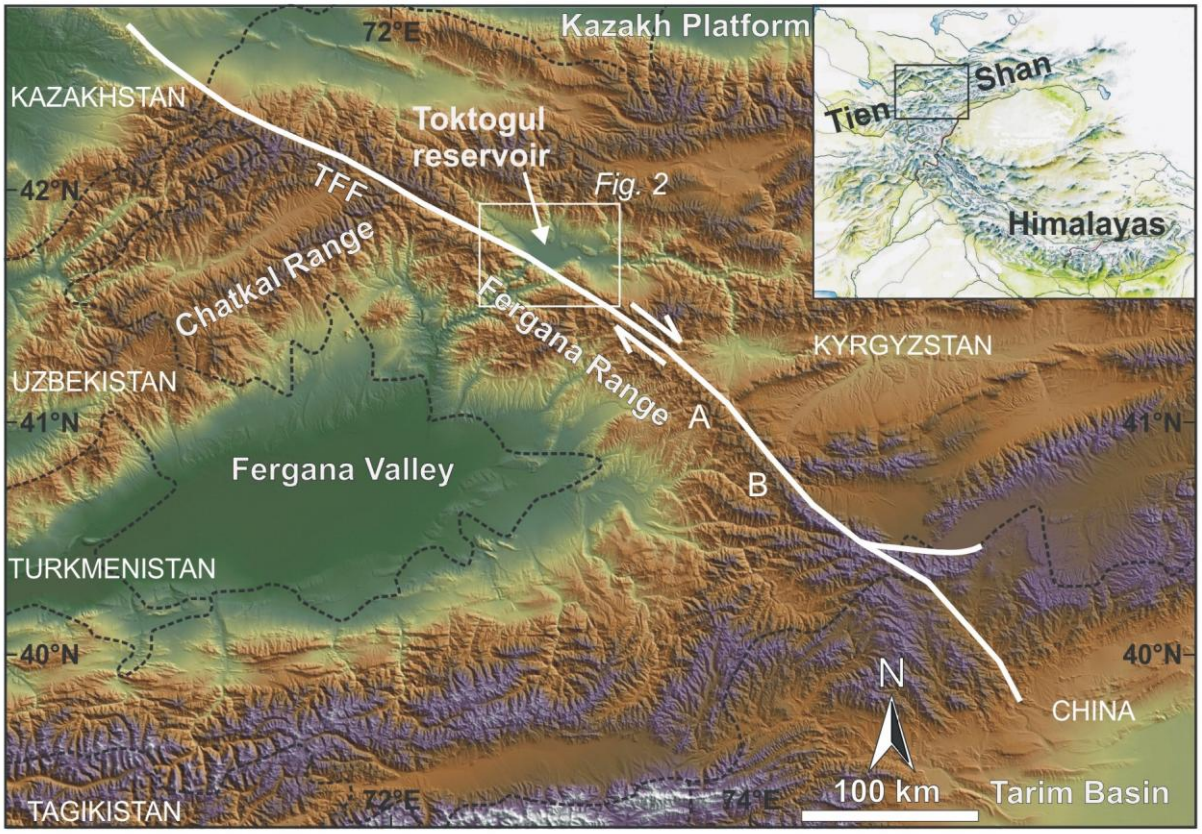

Tibaldi et al., Fig. 1

Shaded relief map of the Tien Shan mountains of central Asia. The dominant East-West structural orientation of the mountain ranges is crosscut by the prominent NW-SE-striking Talas-Fergana Fault (TFF), over 700 kilometres in length. This fault system affects Kazakhstan, Kyrgyzstan and China. Along the fault there is the large Toktogul artificial water reservoir that serves the most important hydroelectrical power station of central Asia. The much larger depression to the SW is the Fergana Valley. A = Kyldau River, B = Pchan River. SRTM from http://srtm.csi.cgiar.org/. The trace of the TFF in Kazakhstan has been taken from Buslov et al. (2003) and Rolland et al. (2013). The trace of the southernmost TFF has been taken from Fu et al. (2010) and Rolland et al. (2013).

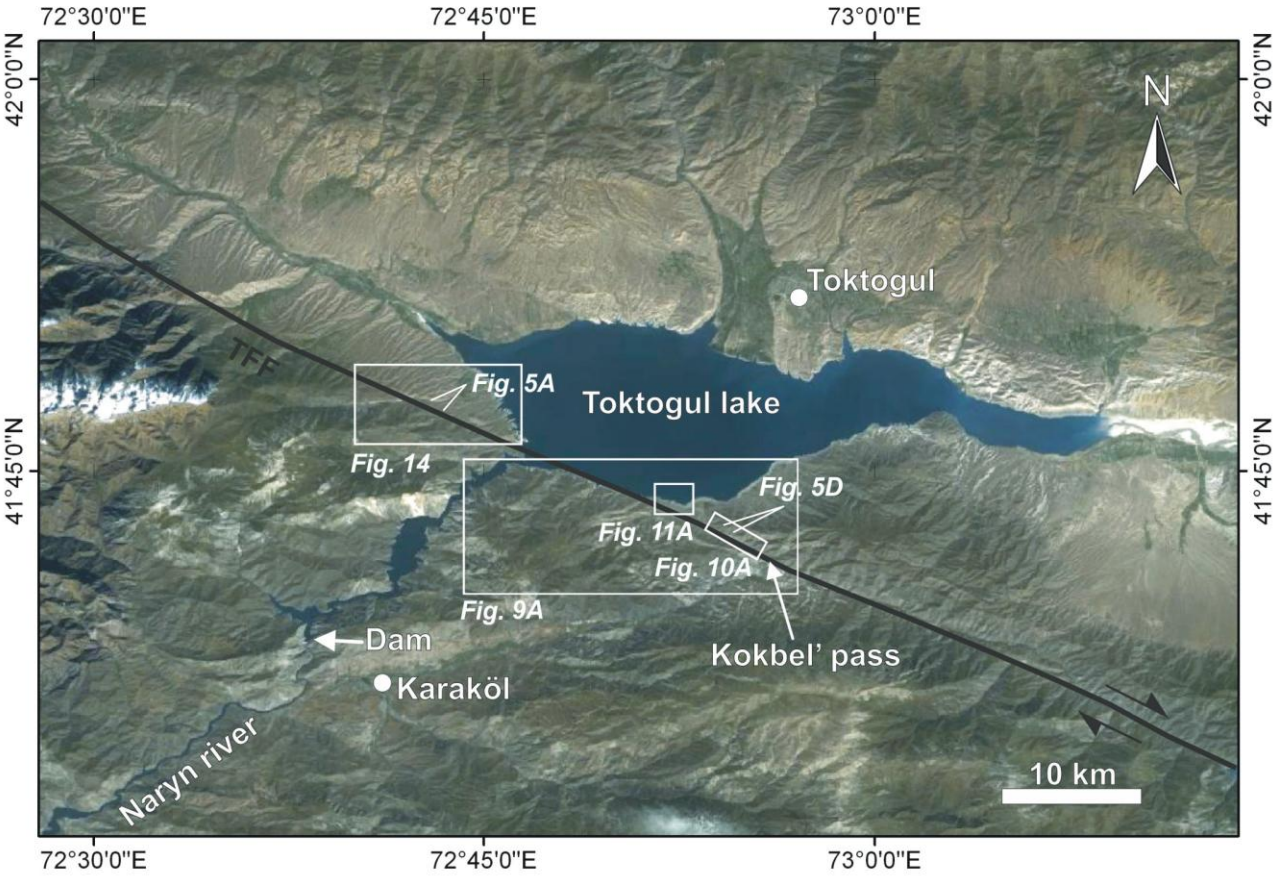

Tibaldi et al., Fig. 2

Satellite image (Google Earth) showing the studied segment of the Talas-Fergana Fault (TFF) in Kyrgyzstan (location in Fig. 1), whose quite continuous surface trace has a strike ranging N116° to N138° from NW to SE. In the northwestern and southeastern parts of this segment the fault trace runs mostly along the valley bottoms, whereas in the central part the fault trace can be followed along mountain slopes (cfr. Fig. 5). Boxes and photo view angles show location of next figures.

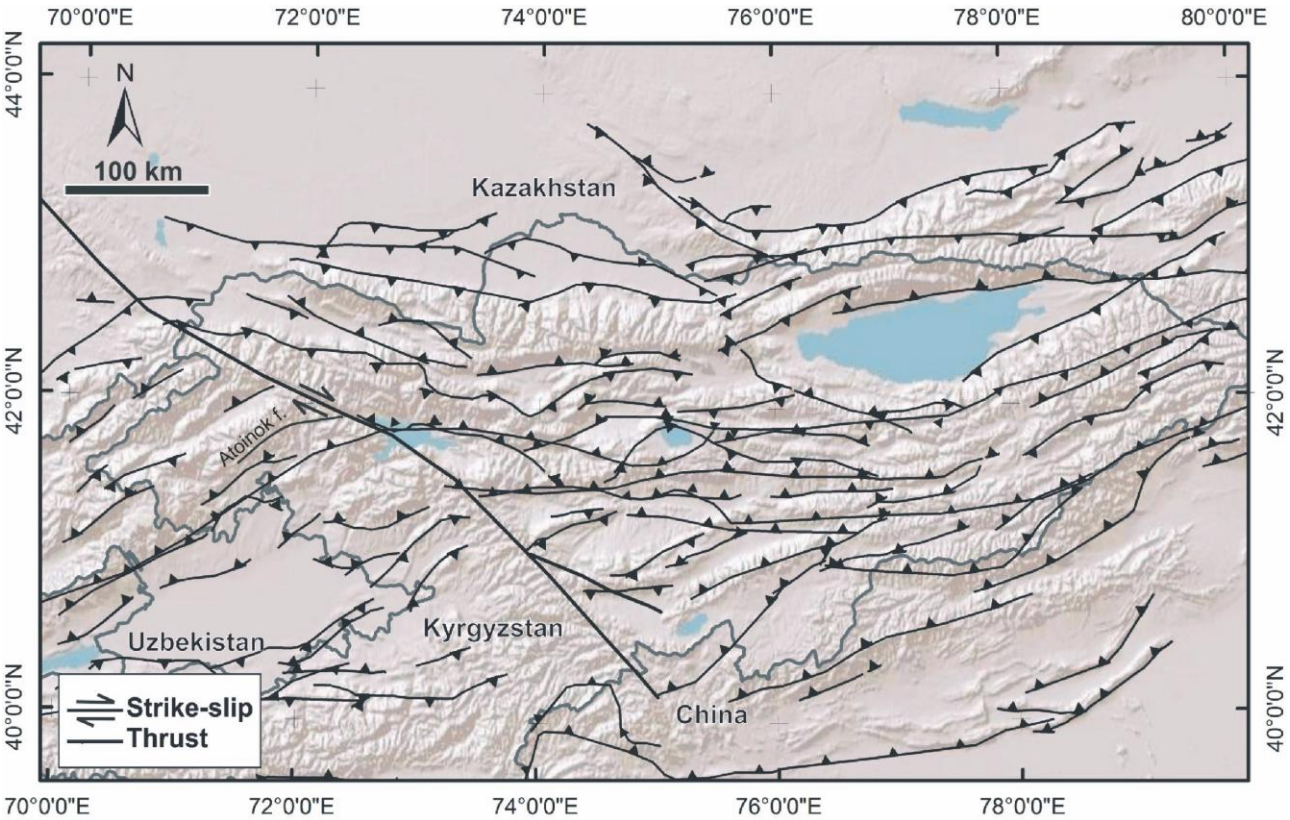

Tibaldi et al., Figure 3

Map of the main Quaternary faults of central Tien Shan. Note the presence of the unique NW-SE-striking right-lateral strike-slip Talas Fergana fault, surrounded by several about E-W-striking reverse faults. Modified after Tapponnier and Molnar (1979), Ghose et al., (1998), Thompson et al. (2002).

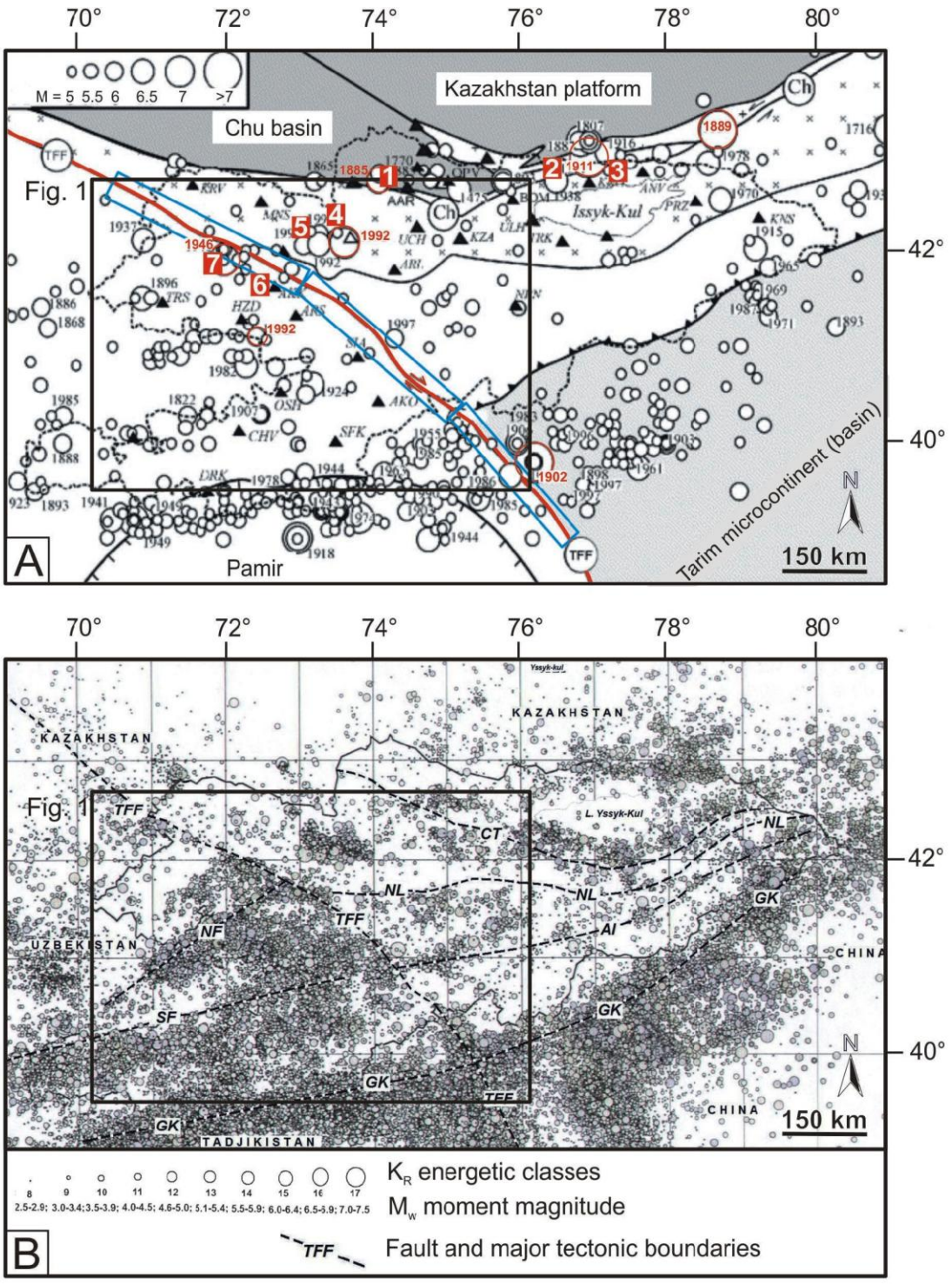

Tibaldi et al., Figure 4

A. Main historic seismic events (1475-1997) around the Talas-Fergana Fault (TFF, in red), and location of earthquake-triggered slope failures (see text for details): 1Kyrgyz Range; 2 = Chon Kemin valley; 3 = Chon Aksu valleys; 4 = Suusamyr valley; 5 = Suusamyr Ranges; 6 = Mailuu-Suu valley; 7 = Sarychelek lake. Highlighted in red are the epicentres of the Chilik (1889), Kashgar (1902), Kemin (1911), Chatkal (1946), Kochkor-Ata (1992) and Suusamyr (1992) earthquakes. Blue boxes locate the three segments (northwestern, central and southeastern) of the TFF for which the peculiarities of the seismic regime were examined. Modified after Buslov et al. (2003), integrated with Kopnichev and Sokolova (2003). *B*. Instrumental seismicity recorded between 1960 and 2008 in central Tien Shan. TFF = Talas Fergana Fault, NF = Northern-Fergana Fault, GK = Ghissar-Kokshaal Fault, AI = Atbashi-Inylchek Fault, NL = Nikolaev Line (Fault). Base maps are from the Kyrgyz Institute of Seismology (KIS) archive. Boxes in both maps locate the area of Fig. 1.

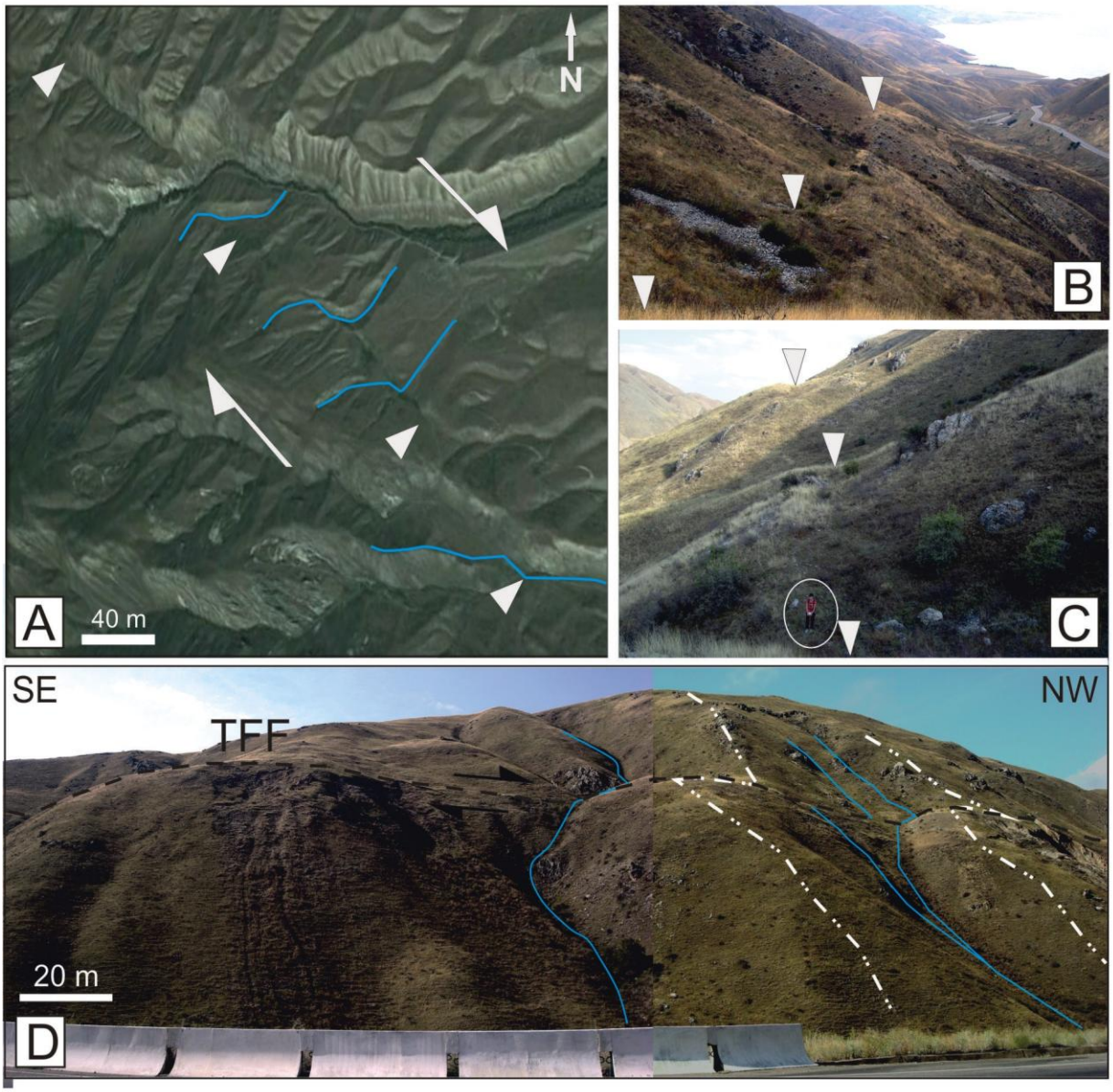

Tibaldi et al., Fig. 5

A. Example of the Talas-Fergana Fault segment where the surface fault trace (triangles) runs parallel to the local slope contour lines, with river gullies (blue lines) systematically offset in a right-lateral sense. Location in Figs. 2 and 14. View towards North, Google Earth image. *B*. and *C*. Photos showing uphill facing scarps ,i.e. facing to the SW, in part due to a small component of uplift of the NE tectonic block (man for scale in circle), *D*. Example of the Talas-Fergana Fault segment located southeast of the Toktogul water reservoir, where it can be appreciated the continuous surface trace (segmented black line, TFF) and the systematic right-lateral strike-slip offset of gullies (blue lines) and of water divides (point and dash lines). Location in Fig. 2.

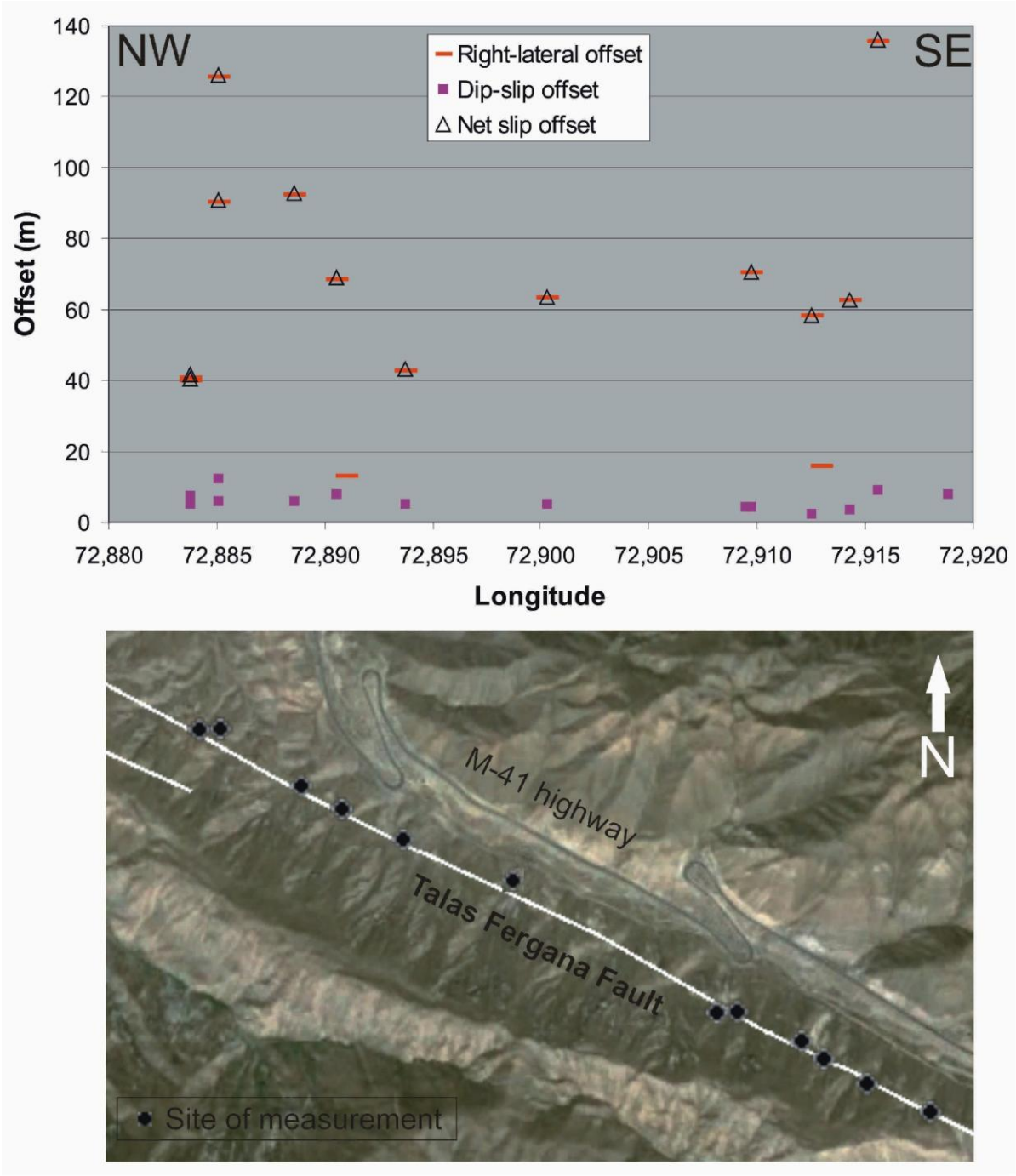

Tibaldi et al., Figure 6.

Cumulative offset measured in the field along the segment of the Talas-Fergana fault between Toktogul Lake and Kokbel' Pass. The right-lateral strike-slip and dip-slip components, and the net slip are shown. The amounts of offset of river gullies and drainage divides are plotted against the distance along fault strike. Inset shows the location of measurement sites along the fault trace, from NW to SE.

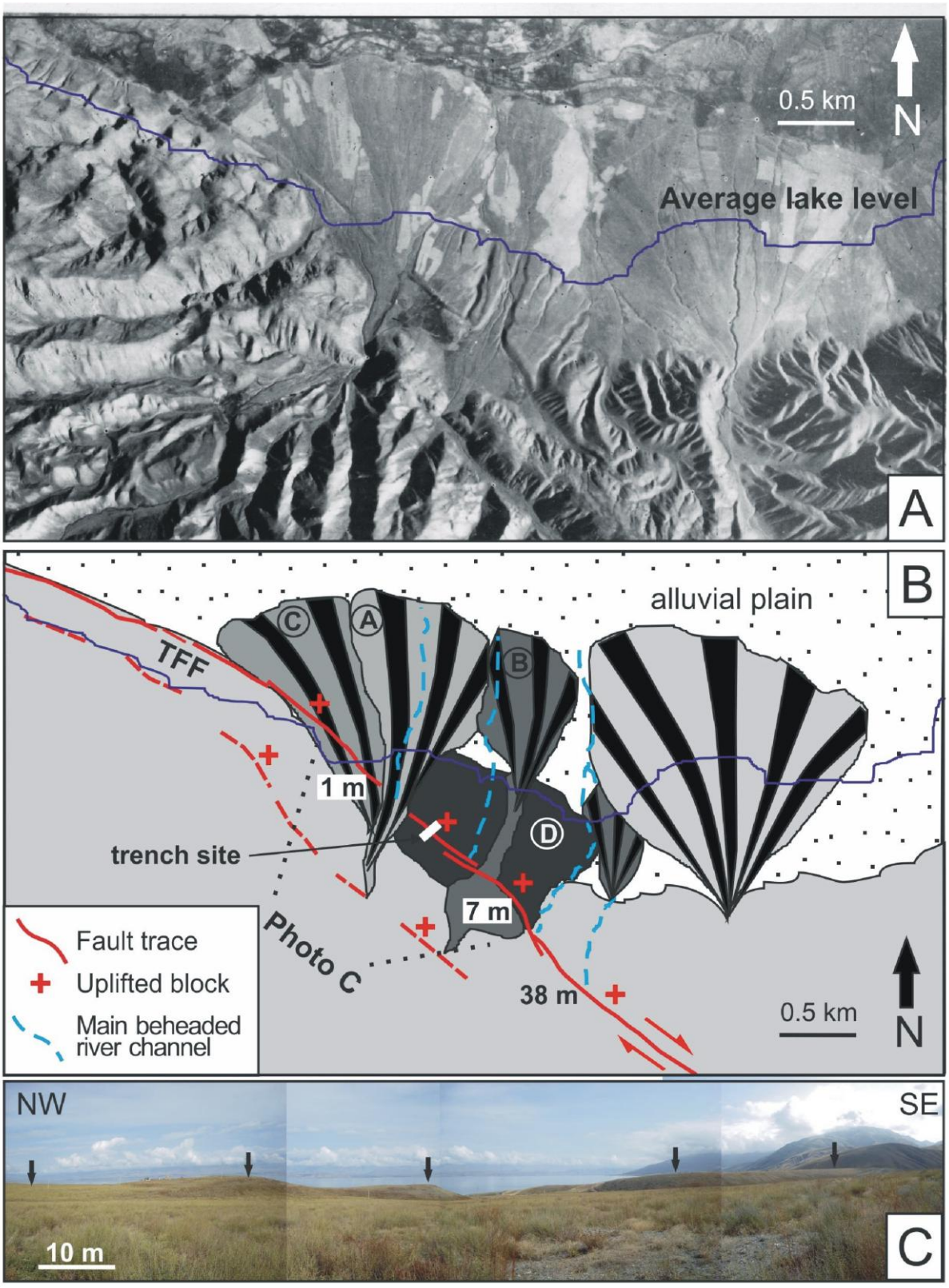

Tibaldi et al., Figure 7

A. Aerial photo taken before the reservoir creation and *B*. its interpretation, integrated also with field data showing a series of Quaternary alluvial fans offset by the TFF (from the oldest fan "D" to the youngest "A"). Numbers refer to the different fault scarp heights that are consistent with the relative age of the alluvial fans. Location in Fig. 10A. *C*. Field photo of the fault scarps indicated by arrows.

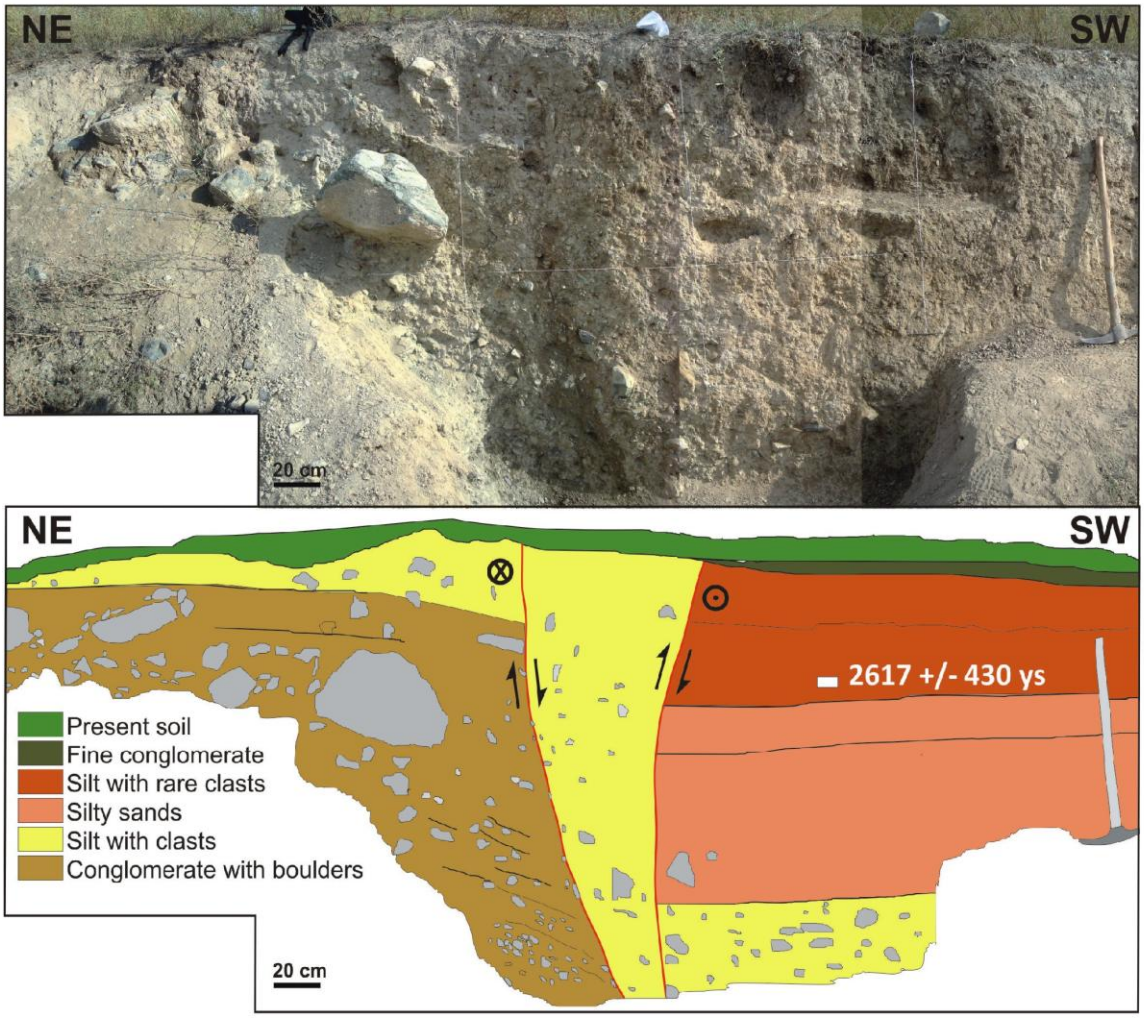

Tibaldi et al., Figure 8.

Photo (*A*) and interpreted log (*B*) of the trench that has been excavated along the newly-recognized fault trace cutting the Quaternary alluvial fans. Age obtained by Optically-Stimulated Luminescence. Location in Figure 7B.

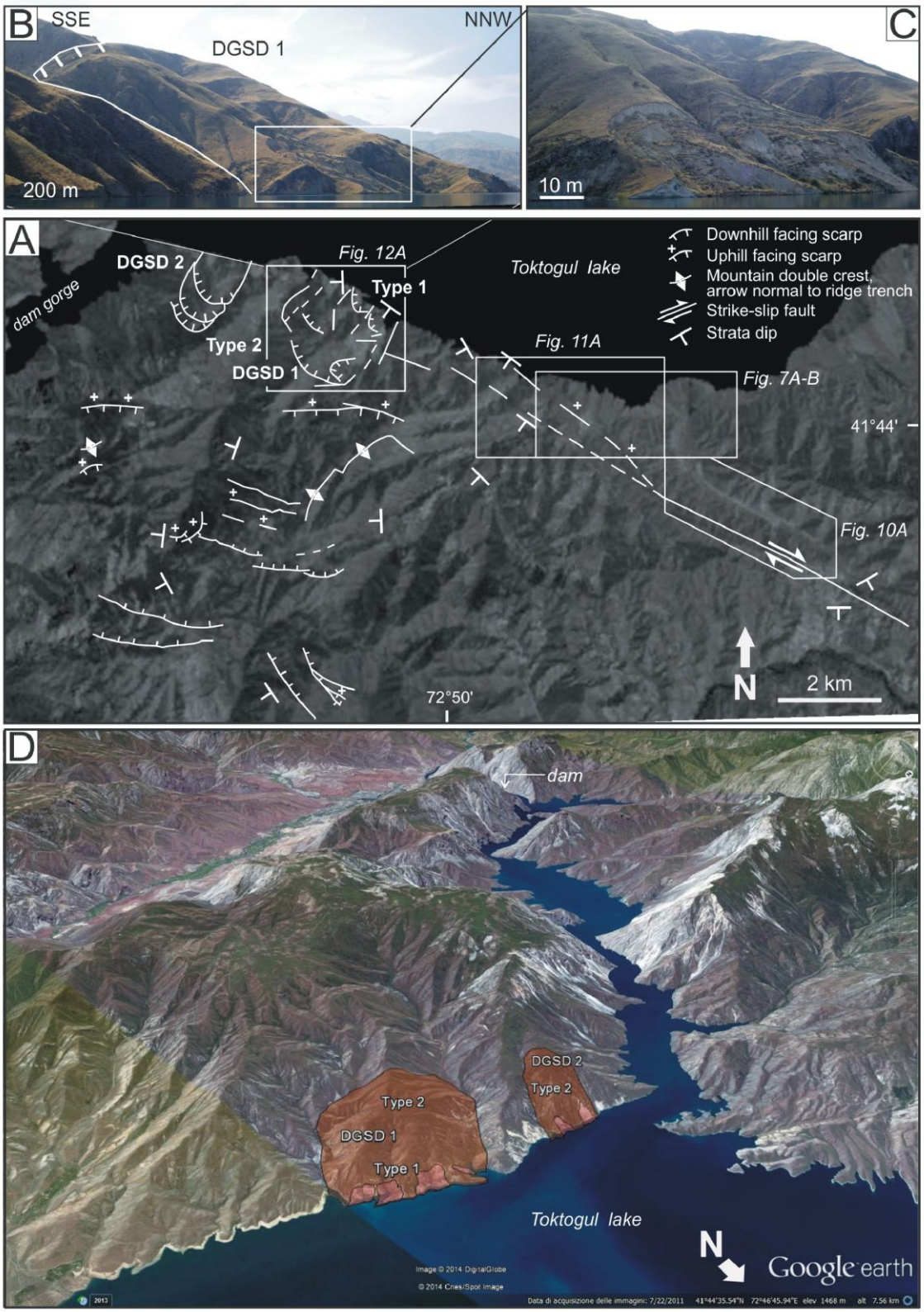

Tibaldi et al., Fig. 9

A. Map of the faults surveyed along the Toktogul reservoir coast, on the prosecution of the surface trace of the Talas-Fergana Fault (location in Fig. 2 and Fig. 10A). These faults might represent Riedel and Riedel 1 shears, respectively, of the main Talas-Fergana Fault, as in the classical simple shear model shown for comparison. *B.* Schmidt's stereogram, lower hemisphere, of the structures found at the studied outcrop. Here faults strike NW-SE and NNE-SSW, and show transcurrent-oblique (transtensional) motion. The line with diverging arrows represents the orientation of the recent fissure. *C.* Photo and interpretation of the studied outcrop. *D.* Photo and interpretation of a close-up on fissures.

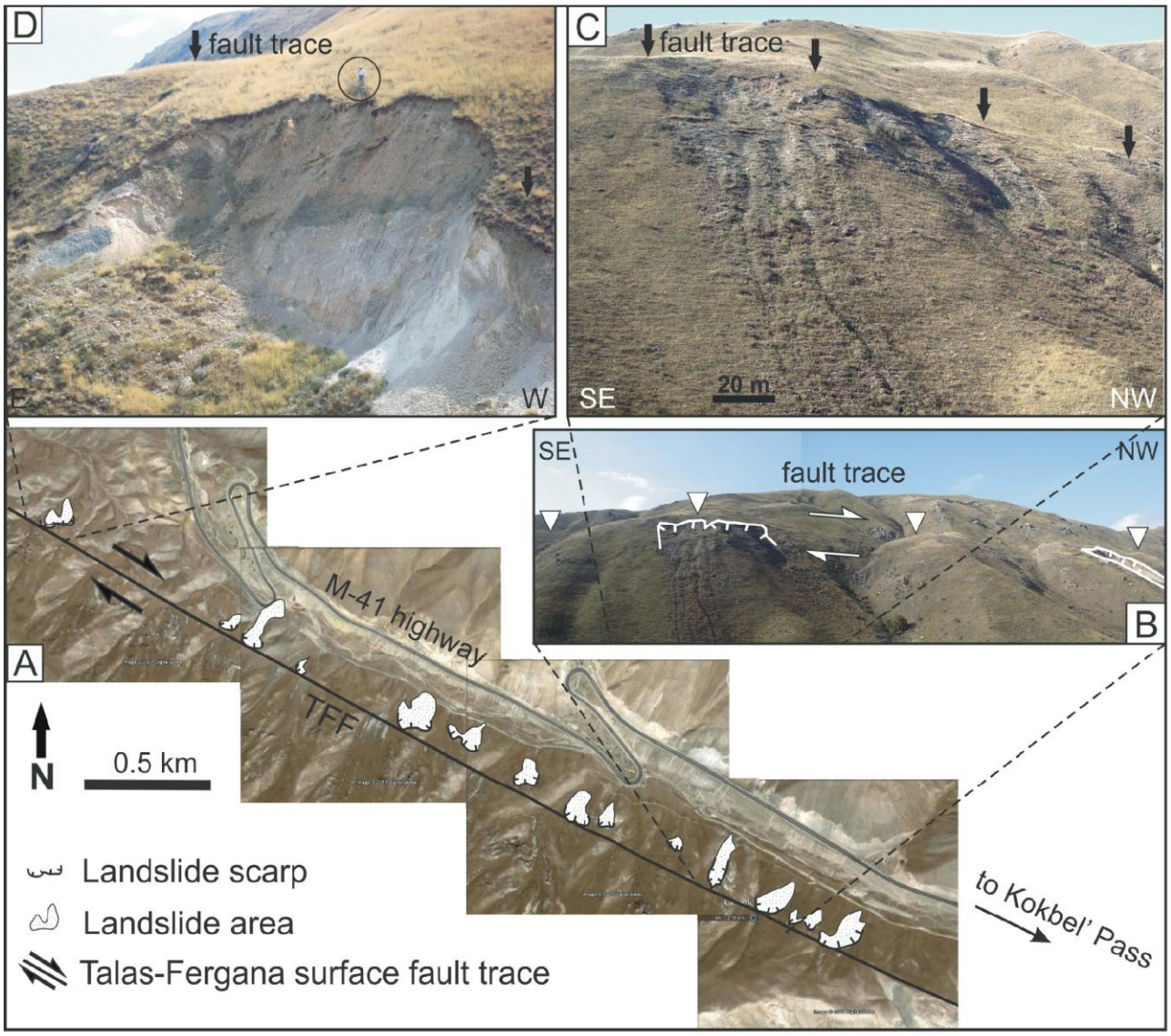

Tibaldi et al., Figure 10

A. Map of the Talas-Fergana Fault trace close to the Toktogul water reservoir (Location in Fig. 2). Note that a branch of the main fault cuts across a Quaternary alluvial fan. Crosses indicate the relative upthrown fault block. To the northwest the fault trace is replaced by a series of recent and active landslides. These comprise surficial slope failures (*Type 1*) and deep-seated gravity slope deformation (DGSD, *Type 2*). DGSD 1 and DGSD 2 are the largest and most recent zones of deep instability that we have found. *B*. Photo of DGSD 1, taken from a boat. *C*. Photo of the shallow active landslide located at the foot of the DGSD 1. *D*. Perspective view (Google Earth) from the NE of *Type 1 and Type 2* instabilities.

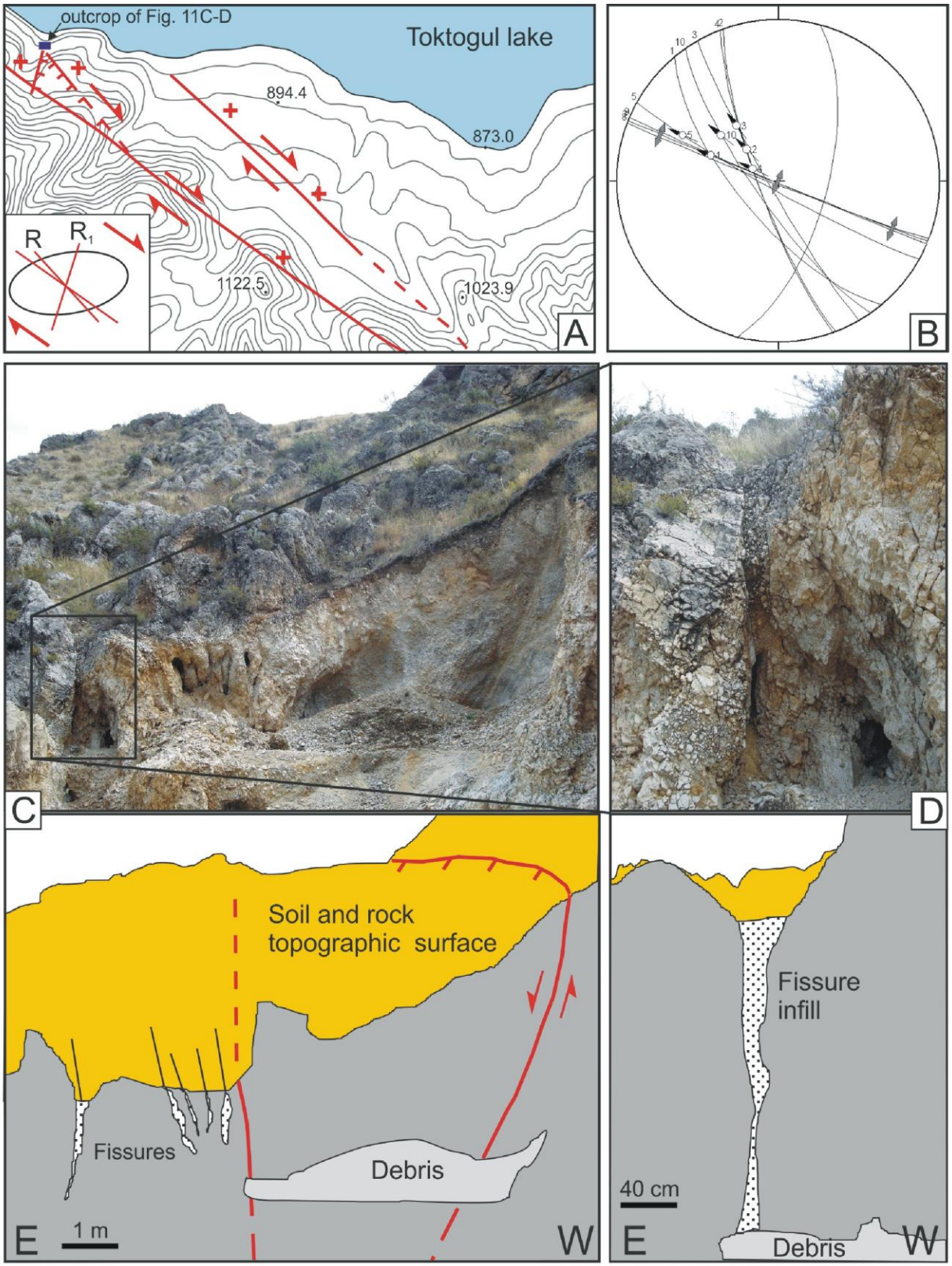

Tibaldi et al., Figure 11

A. Map view over a Google Earth image of the Talas-Fergana Fault (TFF) segment located southeast of the Toktogul water reservoir, where several landslides are aligned along the fault trace, also affecting the M-41 international highway. Location in Fig. 2. B. How the slope affected by landslides appears to the SE of Fig. 10A. Arrows indicate the fault trace. C. Close-up on the slope failure of Fig. 10B. This slope failure involved the Quaternary deposits and the first metres of the hard rock substrate. D. Close-up view of the slope failure affecting the NW area of Fig. 10A. This failure involved also the weathered hard rock substrate for a maximum depth of 30 m of the slip plane. The circle indicates a man for scale, and the arrow the fault trace.

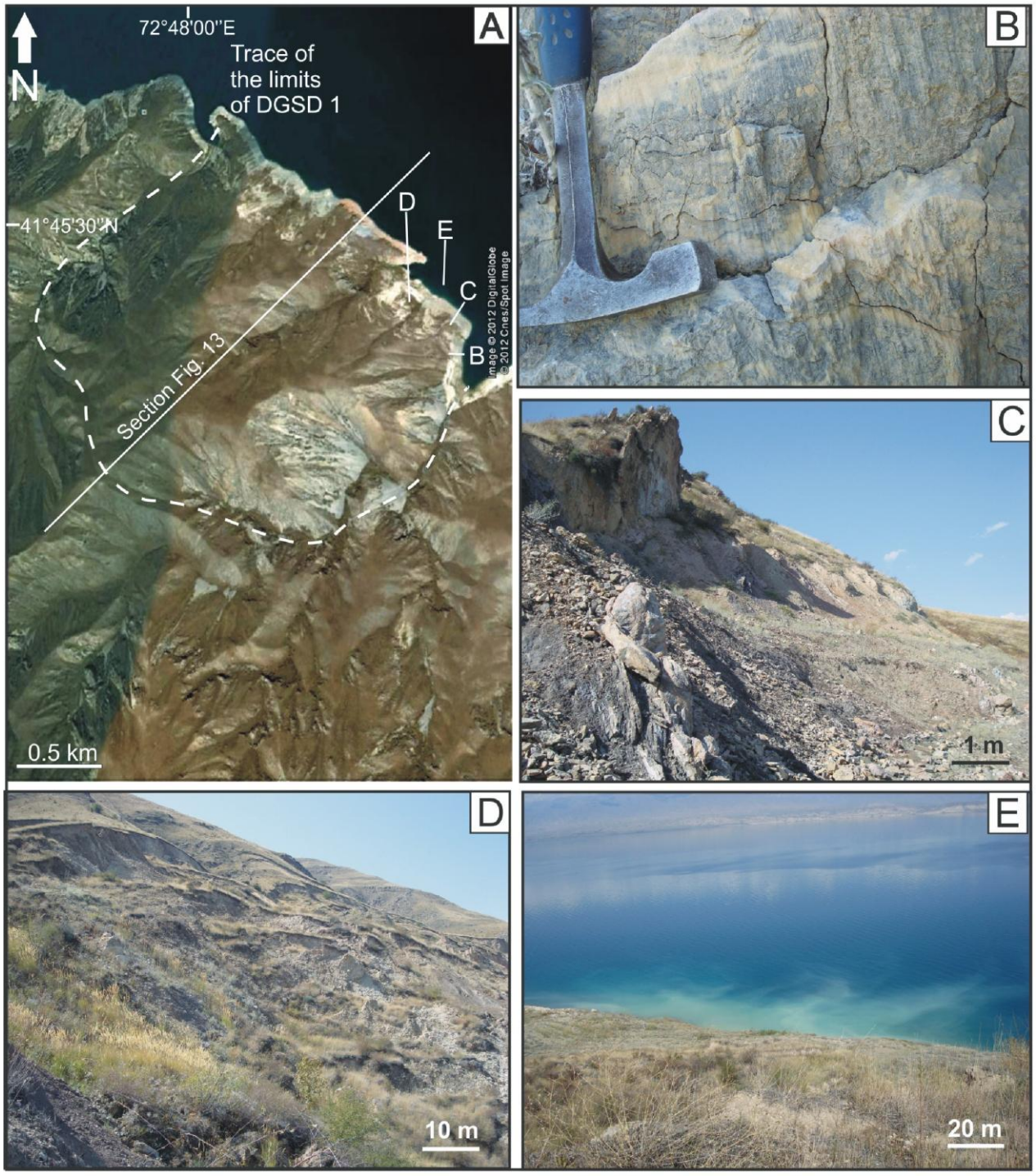

Tibaldi et al., Fig. 12

A. Google Earth image representing the DGSD 1 (see Fig. 10A). Letters locate the following photos, and the trace of the geological cross-section of Fig. 13 is also indicated. *B*. Photo of one of the several rotated reverse faults, with evident striae, that characterise the rock units. *C*. The lowermost part of the outcropping rock succession is characterised by slight metamorphism and pervasive fracturing. *D*. General view of the lower active landslide. *E*. Below the lake level, a wide plume of white water indicates the presence of an underwater spring probably located along the slip plane of the lower active landslide of Figure 12D.

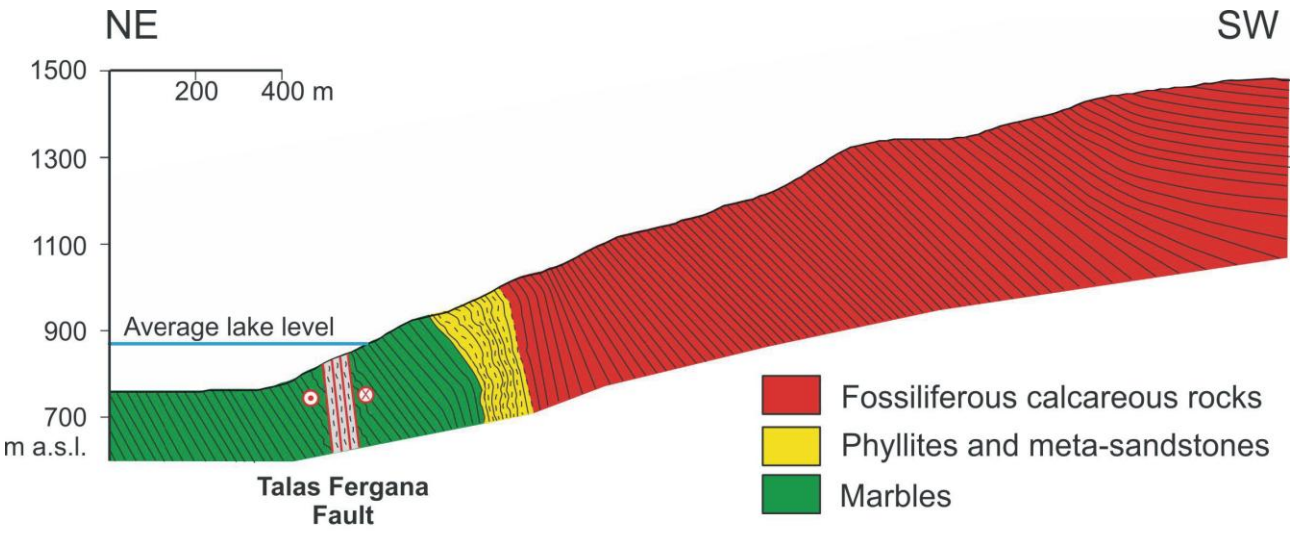

Tibaldi et al., Figure 13.

Geological cross section of DGSD 1 based on geological and structural field data by the authors. Section trace is in Figure 12A.

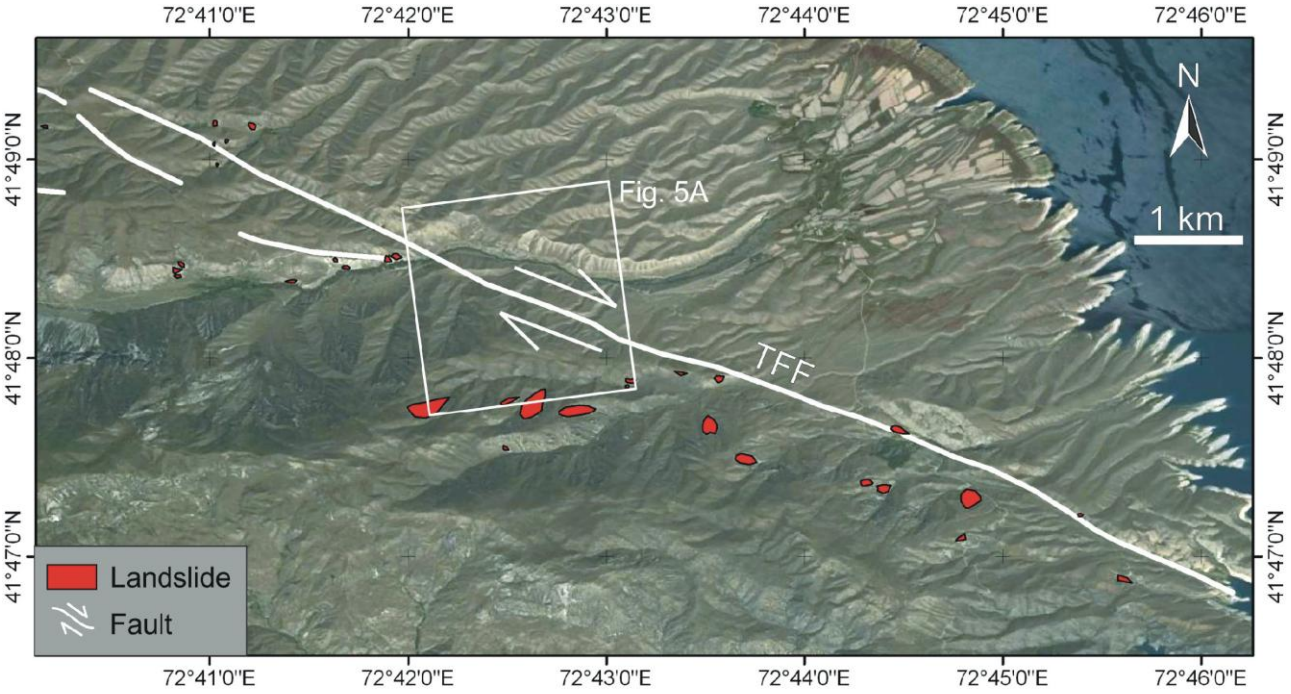

Tibaldi et al., Figure 14

Northwest of the Toktogul lake (location in Fig. 2), the surface trace of the TFF is again continuous with a few subsidiary parallel and sub-parallel faults. Along the fault zone, 33 landslides have been recognized, mostly surficial (*Type 1*). Four landslides are aligned exactly along the fault trace, while all the others are located at a distance < 1.5 km from the fault. Box locates Fig. 5A.

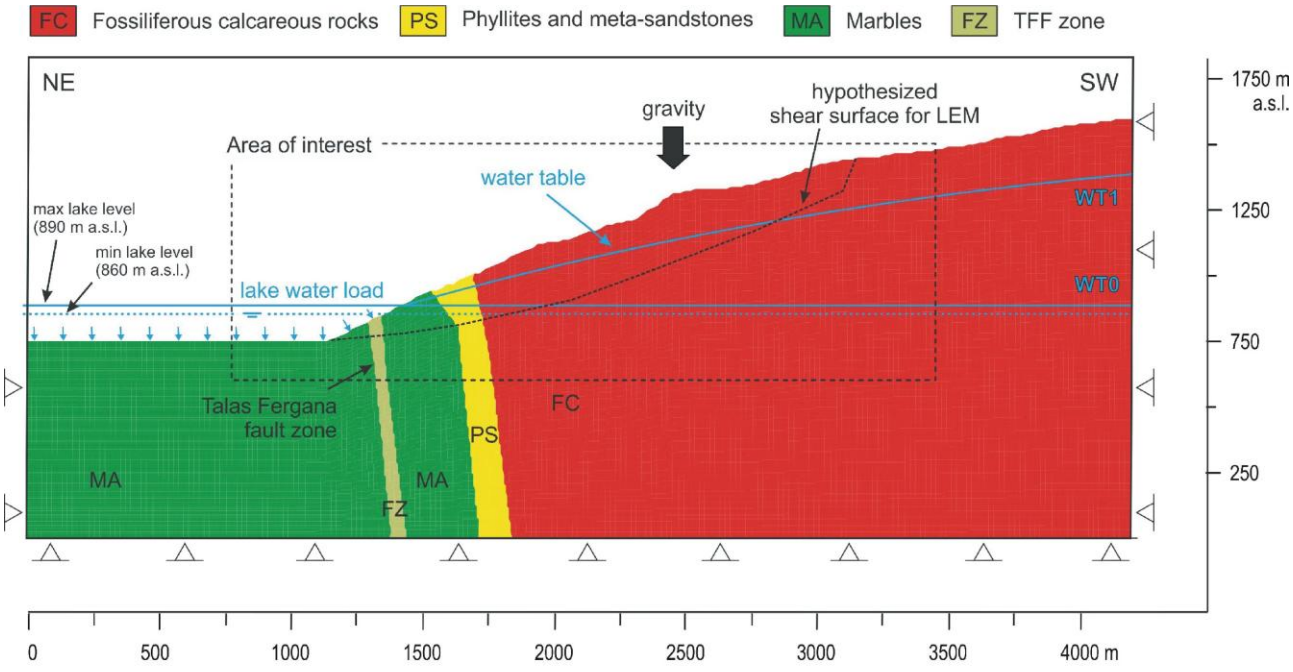

Tibaldi et al., Figure 15.

Geologicaltechnical conceptual model of DGSD 1 (same section trace of Fig. 13) for limit equilibrium and stress-strain numerical analyses, including: main lithotechnical units (properties in Tab. 3), boundary conditions, hydrogeological and gravity settings. FCFossiliferous calcareous rocks, PSPhyllites and meta-sandstones, MAMarbles, FZTalas-Fergana fault zone (fault gauge).

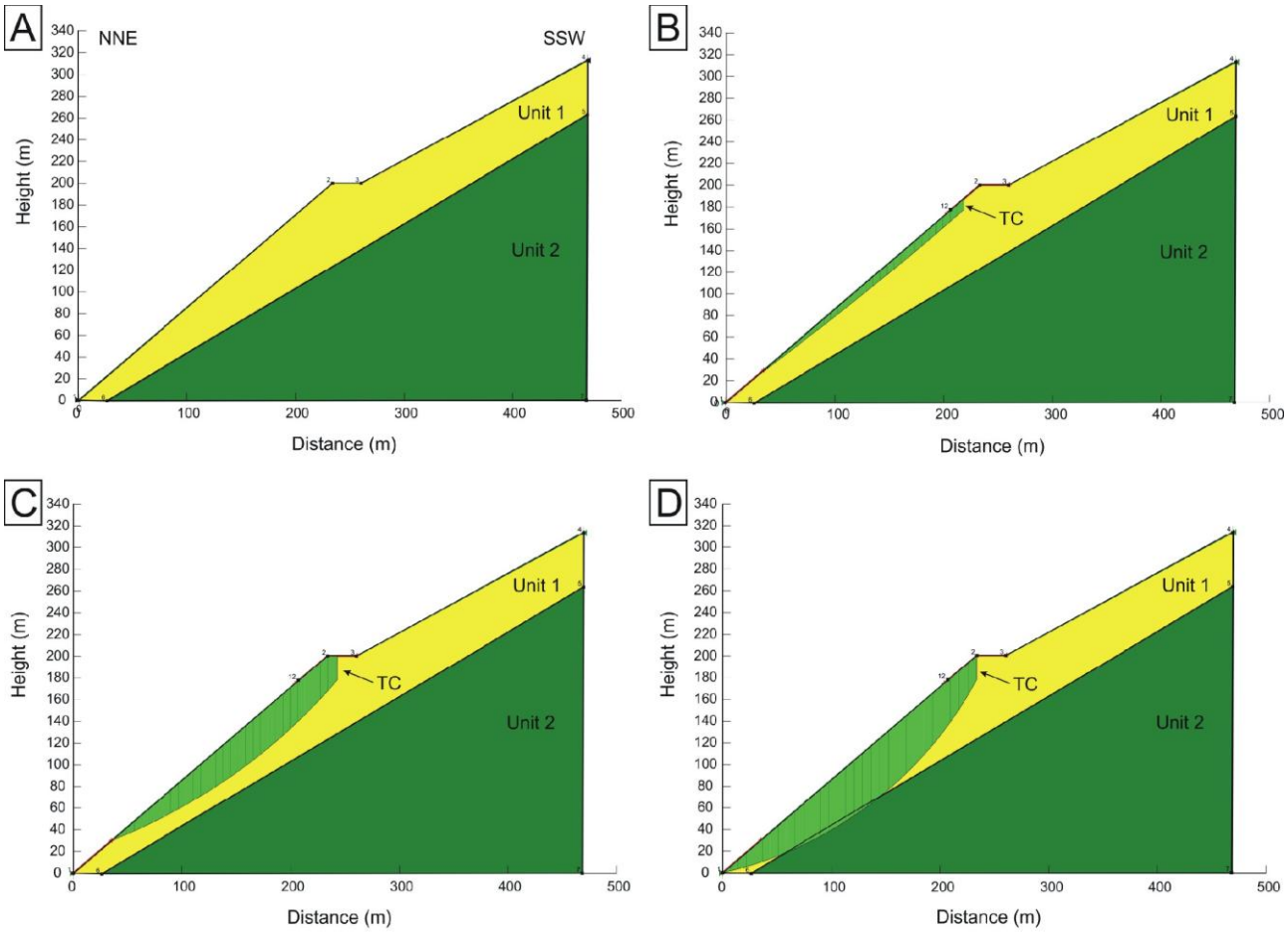

Tibaldi et al., Fig. 16

LEM model and results for *Type 1* instabilities at the Kokbel' Pass, carried out along a representative NE-SW cross-section of the slope (*A*). Unit 1 represents the soil cover, Unit 2 the weathered and fractured bedrock (material properties in Table 2). Result are reported in Table 4. Circular failure surfaces according to Janbu's (1973) method. *B*. shallow surfaces at a depth of 10-15 m show FS < 1 also in dry conditions. *C*. Surfaces involving greater thicknesses (20-30 m) are at limit equilibrium conditions. *D*. Surfaces involving all the soil cover (Unit 1) down to the contact with the weathered and fractured bedrock (Unit 2). FS > 1 unless TC is filled and a seismic coefficient $k_h = 0.15$ is applied, in which case limit equilibrium is reached. TCTension crack, FSFactor of Safety.

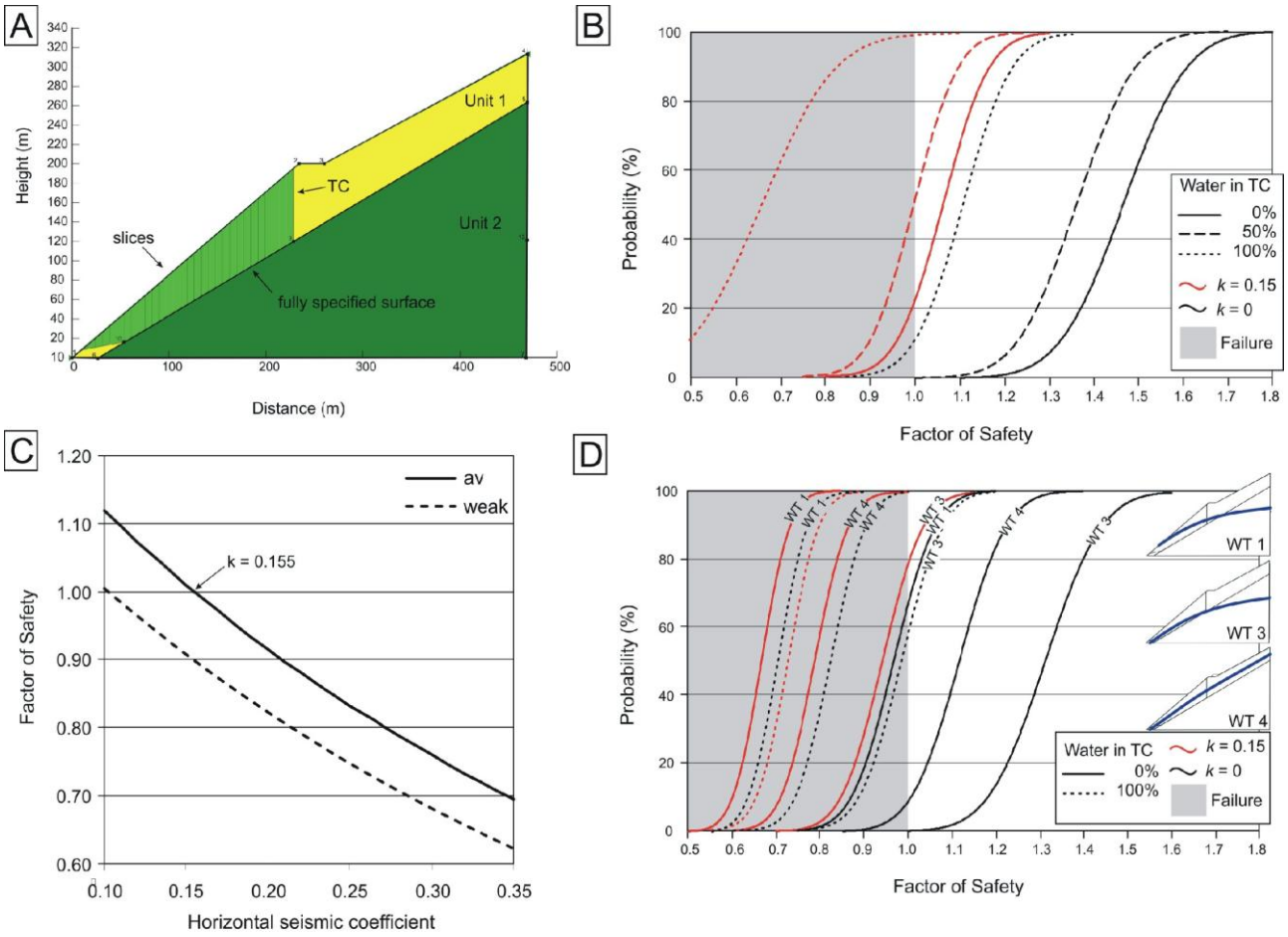

Tibaldi et al., Fig. 17

LEM probabilistic and sensitivity results for *Type 1* instabilities at the Kokbel' Pass. *A*. The fully-specified slide surface is drawn according to field evidence, with the tension crack at the slope break in correspondence with the TFF trace and the slip surface at the contact with the fractured bedrock. Material properties and results in Tables 2 and 4. *B*. Probability distribution function and probability of failure for the dry case in static or pseudo-static ($k = 0.15$) conditions, and TC empty to completely filled. *C*. Results of the sensitivity analyses on k_h in the range 0.1-0.35 with average (Janbu) and lowest (Janbu-L) values of material properties. *D*. Probability distribution function and probability of failure for different hydrogeological conditions in static or pseudo-static ($k = 0.15$) conditions and TC empty to completely filled. TC=Tension crack, WT=Water table (piezometric surface), k=seismic coefficient.

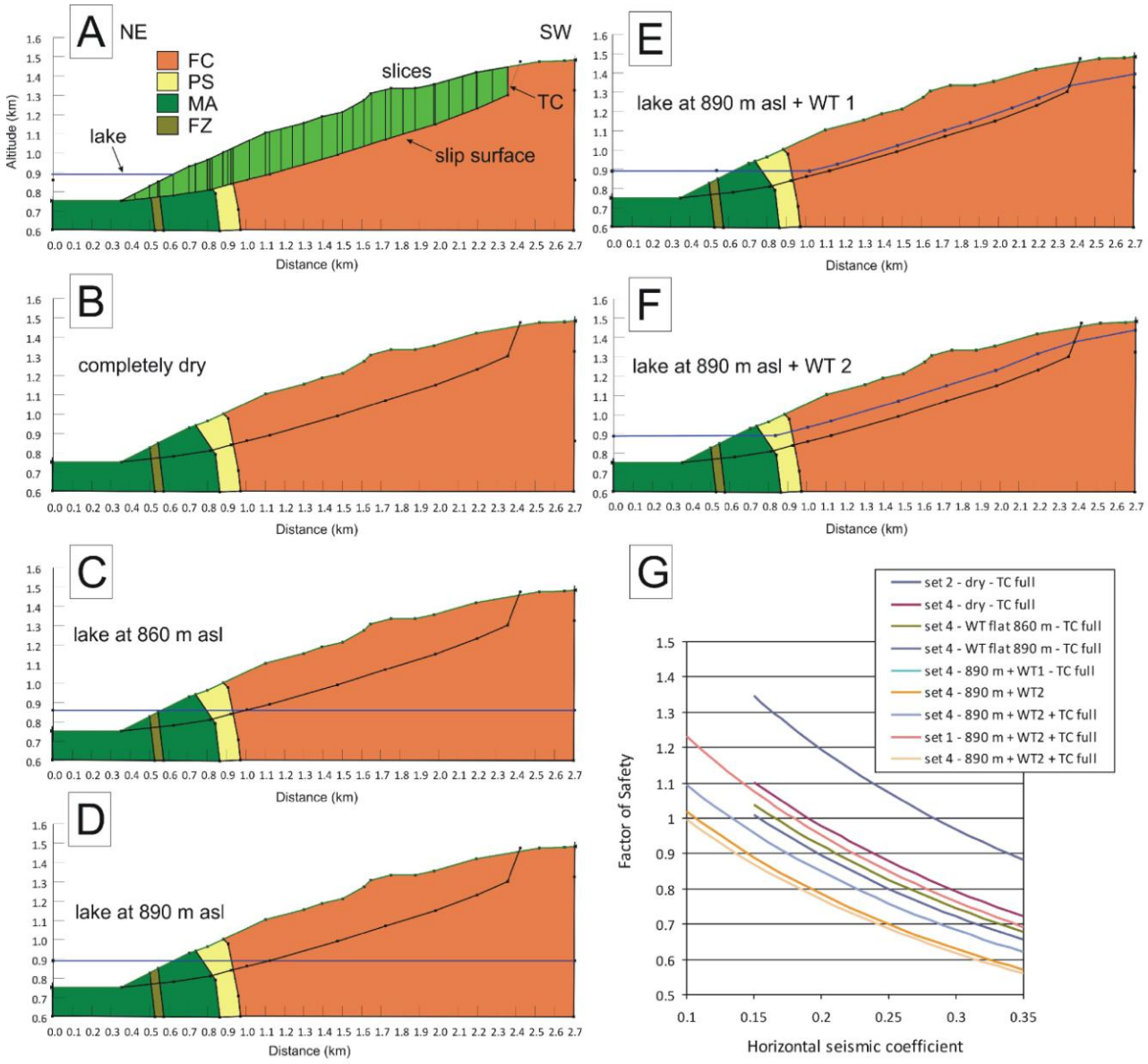

Tibaldi et al., Figure 18

Synthesis of the cases examined by limit equilibrium methods for DGSD 1 in static and pseudo-static conditions. Details and results in Table 5. *A.* Cross section with units, fully specified slip surface, slices and tension crack (TC). Location in Fig. 15. *B.* Completely dry. *C.* Water table coincident with the lake level at 860 m. *D.* Water table coincident with the lake level at 890 m. *E.* Lake level at 890 m, with 20 m head along the shear zone. *F.* Lake level at 890 m, with 80 m head along the shear zone Case E and F are the most critical (FS < 1) when altered material properties and seismic coefficient are introduced. *G.* Results of the sensitivity analysis on *k*. FC=Fossiliferous calcareous rocks, PS=Phyllites and meta-sandstones, MA=Marbles, FZ=Talas-Fergana fault zone (fault gauge), FS=Factor of Safety.

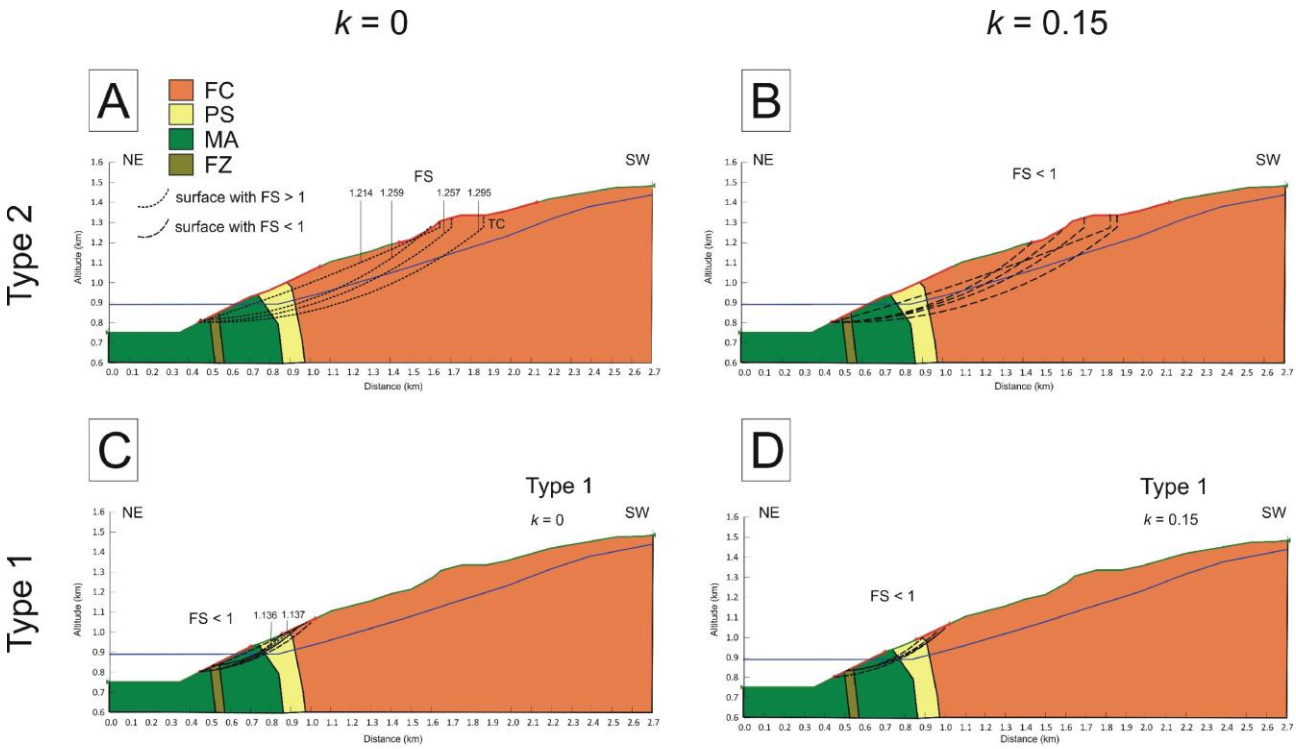

Tibaldi et al., Figure 19

Results for different circular surfaces for *Type 2* (*A-B*) and *Type 1* (*C-D*) instabilities in static (left) and pseudo-static (right, $k_h = 0.15$) conditions. *A. Type 2* instabilities (a number of different possible sliding surfaces is shown) in static conditions have always FS > 1. *B. Type 2* instabilities show a FS < 1 only when a seismic coefficient is applied. *C-D.* On the contrary, *Type 1* instability is greatly affected by the alteration and the saturation of the materials from the reservoir waters, and present failure conditions (FS < 1) even in the absence of seismic loading. FC=Fossiliferous calcareous rocks, PS=Phyllites and meta-sandstones, MA=Marbles, FZ=Talas-Fergana fault zone (fault gauge), FS=Factor of Safety. Piezometric surface is the same WT2 of Figure 18F.

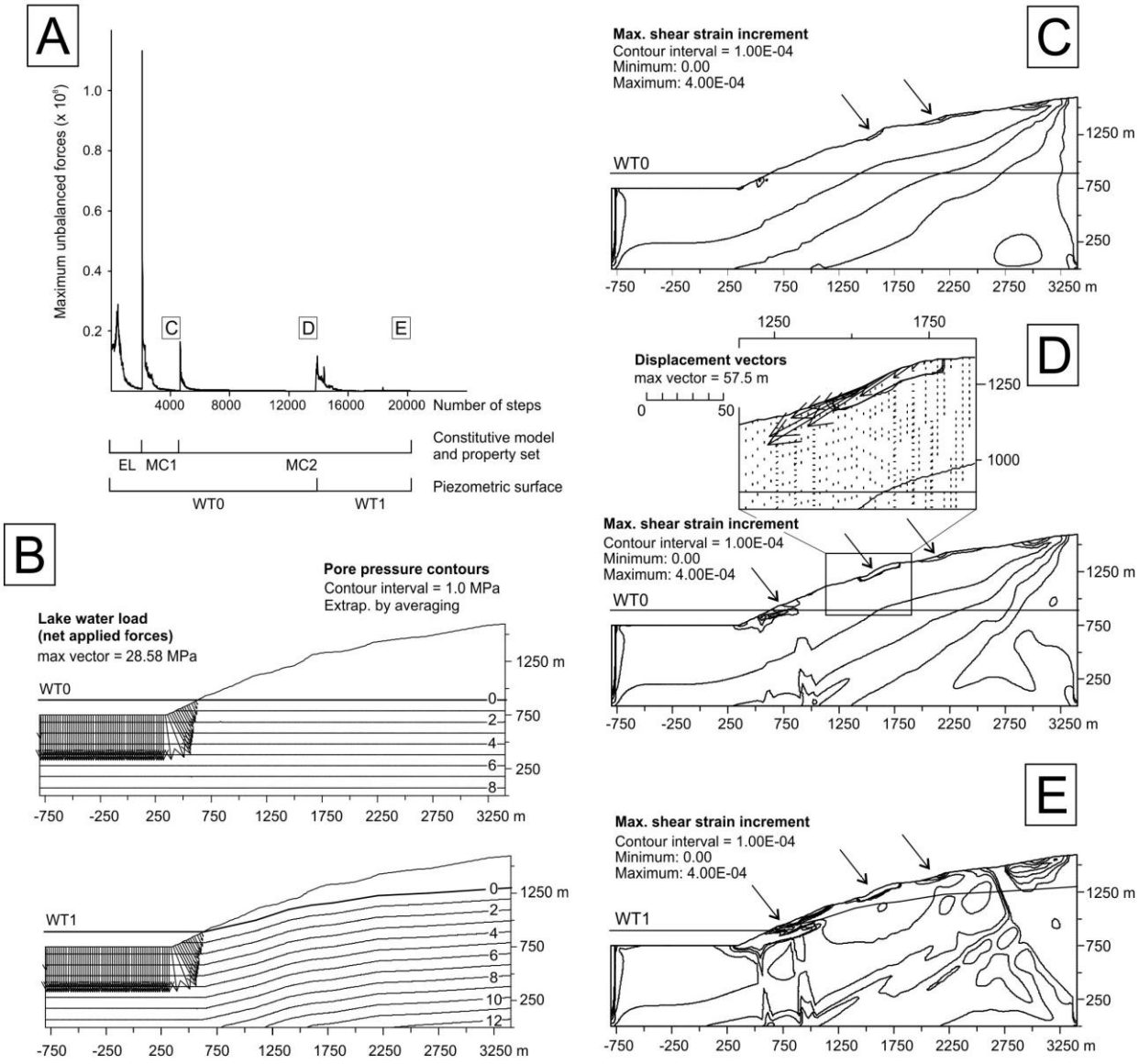

Tibaldi et al., Figure 20

Results of the stress-strain analysis with the finite difference code FLAC 6.0 (Itasca Consulting Group, 2008). *A.* Unbalanced forces resulting from different simulation stages. *B.* Pore pressure distribution, water table and lake water load on submerged free surfaces. WT0 = water table coincident with the lake level at 890 m a.s.l., WT1 = convex-shaped water table. C. Second stage at equilibrium, with Mohr-Coulomb properties (MC1): contours of shear strain increment (SSI). No relevant overall deformation mechanism develops, although incipient shallow concentrations of SSI are evident at slope breaks (outlined by arrows). *D.* Third stage at equilibrium, with degraded Mohr-Coulomb strength and deformability properties (MC2): the contours of shear strain increment coupled with displacement vectors (inset) highlight the development of relatively small shallow-seated areas of instability, marked by yield in shear and consistent with *Type 1* instabilities observed in the field. E. A rise in the piezometric level from WT0 to WT1 leads to a general enlargement of the areas affected by *Type 1* instabilities, but do not evidence the development of a global failure mechanism

Table 1. Data on offsets of river gullies and water divides along the trace of the Talas Fergana fault.

Latitude	Longitude	Right-lateral offset (m)	Dip-slip offset (m)	Net offset (m)	Pitch angle (°)	Offset landform	Distance along fault (m)
41.72626	72.884	40.91	7.52	41.59	10.4	Crest	0
41.72626	72.884	40.18	5.11	40.50	7.2	Gully	0
41.72628	72.885	125.62	12.47	126.24	5.7	Crest	106.9413
41.72628	72.885	90.62	6.13	90.82	3.8	Gully	106.9413
41.72414	72.889	92.56	5.92	92.75	3.7	Gully	484.7834
41.72328	72.891	68.72	8.06	69.19	6.7	Crest	674.5031
41.72328	72.891	13.26				Gully	674.5031
41.72328	72.891	68.72	8.11	69.2	6.7	Gully	674.5031
41.72215	72.894	42.82	5.21	43.14	6.9	Gully	964.7368
41.7214	72.900	63.32	5.06	63.52	4.6	Gully	1519.7976
41.7159	72.909		4.39			Crest	2496.2974
41.71591	72.910	70.48	4.24	70.61	3.5	Gully	2517.96256
41.71488	72.913	15.70				Gully	2778.53546
41.71488	72.913	58.14	2.33	58.18	2.3	Gully	2778.53546
41.71427	72.914	62.75	3.57	62.77	3.3	Gully	2938.40446
41.71338	72.916	135.77	9.23	136.02	3.9	Gully	3084.88506
41.71236	72.919		7.90			Gully	3379.27656
Average		73.89	6.35	74.19	5.3		

Table 2. Input data for limit equilibrium analyses of Type 1 landslides at the Kokbel' Pass. Ranges as introduced in the probabilistic analysis, in brackets the deterministic values. Pseudo-cohesion was observed in situ for Unit 1.

Name	Type of deposit	Properties		
		Unit weight γ (kN/m^3)	Friction angle ϕ' (°)	Cohesion c' (kPa)
Unit 1	Poorly graded gravel, gravel-sand mixture, little or no fines (cohesionless)	22	35-45 (38)	0
Unit 2	Strongly weathered weak rock blocks in sandy clay matrix (weakly cohesive)	22	35-45 (38)	10-50 (20)

Table 3. Geotechnical characterization of the geological-technical units involved in DGSD 1. In bold, values used in FDM stress-strain analysis: in the "altered" set, the fault zone is considered as an extremely porous and cohesionless gauge material. FC—Fossiliferous calcareous rocks, PS—Phyllites and meta-sandstones, MA—Marbles, FZ—Talas-Fergana fault zone.

Properties	Units	Geological-technical units						
		FC		PS		MA		FZ
		intact	*altered*	*intact*	*altered*	*intact*	*altered*	
Uniaxial compressive strength (UCS)	MPa	25–50 (**40**)	1–5 (**5**)	10–20 (**15**)	<1 (**1**)	40–60 (**45**)	1–5 (**5**)	5 (**5; 1**)
Dry unit weight (γ_d)	kN/m^3	26		26		26		20
Cohesion (c')	kPa	50–200 (**50**)	0–10 (**5**)	100–300 (**100**)	0–20 (**5**)	100–300 (**100**)	0–10 (**5**)	0-10 (**10; 0**)
Base friction angle (ϕ')	°	32 (**32**)	25 (**27**)	35 (**35**)	20–25 (**25**)	32 (**32**)	27 (**30**)	28-30 (**30; 28**)
Poisson's ratio (ν)	-	0.29–0.30 (**0.29**)		0.26-0.27 (**0.26**)		0.26–0.27 (**0.26**)		0.26–0.27 (**0.26**)
Young's modulus (E)	GPa	20–30 (**20**)	10–20 (**10**)	10–20 (**10**)	5–10 (**5**)	30–50 (**30**)	20–50 (**20**)	5-20 (**20; 5**)

Table 4. Results of LEM analysis for Type 1 instabilities at the Kokbel' Pass (cfr. Figs. 15-16). Material properties report the range used for probabilistic analysis, in brackets the values for deterministic trials. WT—water table (piezometric surface), TC—tension crack, FS—Factor of Safety, PF—probability of failure, auto—automatically searched surface.

Fig.	Sliding surface	WT	TC fill (%)	k	FS	PF (%)
16B	surficial sliding (auto)	no	0	0	< 1	-
16C	circular (auto)		0	0	~ 1	-
16D			0	0	> 1	-
			100	0.15	~ 1	-
17B	user-defined (Fig. 16A)	no	0	0	1.394	0
			50		1.295	0
			100		1.054	7.95
			0	0.15	1.011	27.1
			50		<1	56.6
			100		<1	100
-		WT 2	0	0	1.394	0
			100		1.054	7.95
			0	0.15	1.011	27.1
			50		< 1	99.9
17D		WT 3	0	0	1.248	0
			100		< 1	62.5
			0	0.15	< 1	77.6
			100		< 1	100
		WT 1	0	0	< 1	68.05
			100		< 1	100
			0	0.15	< 1	100
		WT 4	0	0	1.062	5.7
			100		< 1	100
			0	0.15	< 1	100
-		WT 6	0	0	< 1	100
		WT 5	0		< 1	100

Table 5. Synthesis of the examined cases for the Type 2 instability DGSD 1 (portrayed in Fig. 18): input data, hydrogeological conditions and Factor of Safety (FS) outcomes, along with sensitivity analysis results. FC—Fossiliferous calcareous rocks, PS—Phyllites and meta-sandstones, MA—Marbles, FZ—Talas Fergana fault zone, WT—water table. γ—unit weight, c—cohesion, ϕ—friction angle. DET—Deterministic, SENS—Sensitivity.

Material properties													**Hydrogeological conditions**			**Seismicity**			**Sensitivity analysis (Fig. 17G)**		
set	**FC**			**PS**			**MA**			**FZ**			**Analysis**	**lake level (masl)**	**WT**	**TC fill (%)**	***k***	**FS**	***k* range**	**critical *k***	**Repres. Fig. 17**
	γ (kN/m^3)	c (kPa)	ϕ (°)	γ (kN/m^3)	c (kPa)	ϕ (°)	γ (kN/m^3)	c (kPa)	ϕ (°)	γ (kN/m^3)	c (kPa)	ϕ (°)									
1	26	50	32	26	100	35	26	100	32	20	10	30	DET	-	-	0	0	2.155			B
													DET	-	-	0	0.15	1.376			
													DET	-	-	100	0	2.091			
													DET	-	-	100	0.15	1.347			
													DET	860	flat	0	0	2.058			C
													DET	890	flat	0	0	2.007			D
													DET	890	WT 1	0	0	1.911			E
													DET	890	WT 2	0	0	1.745			F
													DET	890	WT 2	100	0	1.692			

												DET+SENS	890	WT2	100	0.15	1.077	0.1-0-35	0.18	
2	26	50	32	26	100	35	26	100	32	20	0	28	DET	-	-	0	0	2.154			B
													DET+SENS	-	-	100	0.15	1.346	0.1-0-35	0.29	
													DET	860	flat	0	0	2.057			C
3	26	5	27	26	5	25	26	5	30	20	10	30	DET	-	-	0	0	1.778			B
													DET	-	-	0	0.15	1.126			
													DET	-	-	100	0	1.711			
													DET	-	-	100	0.15	1.103			
4	26	5	27	26	5	25	26	5	30	20	0	28	DET+SENS	-	-	100	0.15	1.102	0.1-0-35	0.2	
													DET	860	flat	0	0	1.679			C
													DET+SENS	860	flat	100	0.15	1.04	0.1-0-35	0.17	
													DET+SENS	890	flat	100	0.15	1.009		0.16	
													DET	890	WT1	0	0	1.546			E
													DET	890	WT1	100	0	1.499			
													DET+SENS	890	WT1	100	0.15	< 1	0.1-0-35	0.14	
													DET	890	WT2	0	0	1.411			F
													DET+SENS	890	WT2	0	0.15	< 1	0.1-0-35	0.11	
													DET	890	WT	10	0	1.36			

														2	0		8			
												DET+SE NS	890	WT 2	10 0	0.15	< 1	0.1-0-35	0.1	

Highlights

- Structural-paleoseismological data show Holocene-recent activity at the Talas-Fergana Fault
- A series of Holocene and active landslides is also aligned along this fault
- A deep-seated landslide with V=1 km^3 is present along the artificial Toktogul lake
- An earthquake with k=0.15 can trigger the collapse of this landslide into the lake
- This failure may induce a tsunami; other minor landslides may affect the M-41 highway